Nano Research

ISSN 1998-0124 CN 11-5974/O4
https://doi.org/10.26599/NR.2026.94908714

Research Article

Cooperation of frustrated Ga···N and Ga···Ga pairs on GaN breaks the linear scaling relationship in propane dehydrogenation

Xi-Yang Yu[1], Han-Xuan Liu[1], Han-Tao Cheng[1], Zheng-Qing Huang[1], Chun-Ran Chang[1,2](✉)

[1] State Key Laboratory of Fluorine & Nitrogen Chemicals, School of Chemical Engineering and Technology, Xi'an Jiaotong University, Xi'an 710049, China

[2] National Innovation Platform (Center) for Industry-Education Integration of Energy Storage Technology, Xi'an Jiaotong University, Xi'an 710049, China

Nano Res., **Just Accepted Manuscript** • https://doi.org/10.26599/NR.2026.94908714

https://www.sciopen.com/journal/1998-0124 on Apr. 6, 2026

Just Accepted

TABLE OF CONTENTS (TOC)

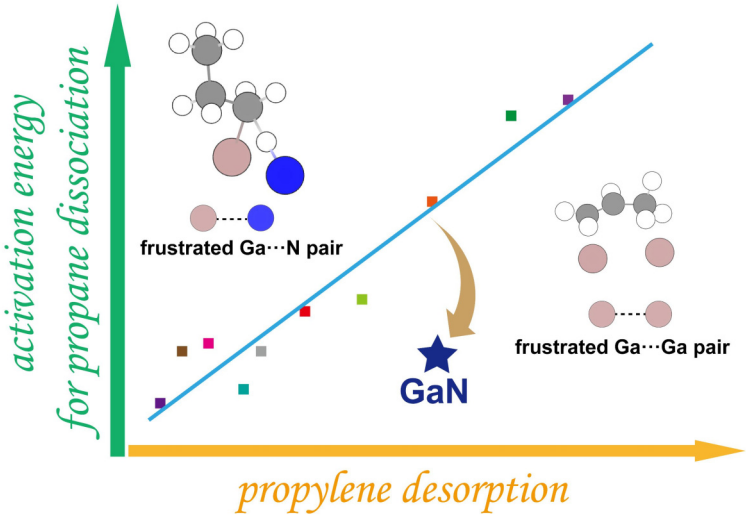

Dual frustrated pairs on GaN surfaces achieve both high catalytic activity and high propylene selectivity for propane dehydrogenation. The Ga···N pairs promote C–H cleavage in propane, whereas Ga···Ga pairs enable facile desorption of propylene.

Nano Research

Open Access

Research Article

Cooperation of frustrated Ga···N and Ga···Ga pairs on GaN breaks the linear scaling relationship in propane dehydrogenation

Xi-Yang Yu[1], Han-Xuan Liu[1], Han-Tao Cheng[1], Zheng-Qing Huang[1], and Chun-Ran Chang[1,2] ✉

[1] *State Key Laboratory of Fluorine & Nitrogen Chemicals, School of Chemical Engineering and Technology, Xi'an Jiaotong University, Xi'an 710049, China*

[2] *National Innovation Platform (Center) for Industry-Education Integration of Energy Storage Technology, Xi'an Jiaotong University, Xi'an 710049, China*

Received: day month year; **Revised:** day month year; **Accepted:** day month year (automatically inserted by the publisher)

✉ Address correspondence to changcr@mail.xjtu.edu.cn

Cite this article: *Nano Research*, 2026, 19, 94908714 https://doi.org/10.26599/NR.2026.94908714

ABSTRACT: Propane dehydrogenation to propylene represents a key route for replacing traditional petroleum-based processes. However, conventional Pt-based catalysts are limited by an intrinsic scaling relationship between C–H activation capability and propylene adsorption strength, such that enhancing catalytic activity would lead to the reduction of propylene selectivity and even coking. Herein, we demonstrate that the cooperative frustrated Ga···N and Ga···Ga pairs on GaN can effectively break the linear scaling relationship. The frustrated Lewis pairs (Ga···N) facilitate the rate-limiting step of the first C–H bond dissociation in propane, with a Gibbs free energy of activation of 1.63 eV, slightly lower than that on the conventional Pt–Sn catalyst (1.81 eV). The frustrated metal pairs (Ga···Ga) are responsible for 1-propyl dehydrogenation, exhibiting weak propylene adsorption and further suppressing the deep dehydrogenation of propylene. Kinetic Monte Carlo simulations based on the overall reaction network indicate that GaN exhibits excellent catalytic activity, with a turnover frequency of 18.33 s^{-1} for propylene production, significantly higher than that of Pt-based catalysts. This study not only elucidates how the cooperation of frustrated Ga···N and Ga···Ga pairs breaks the linear scaling relationship, but also provides insights for the design of novel catalysts for propane dehydrogenation.

KEYWORDS: breaking scaling relationship, propane dehydrogenation, frustrated Lewis pairs, frustrated metal pairs, gallium nitride

1 Introduction

Propane dehydrogenation (PDH) provides a non-petroleum-based route for propylene production by utilizing low-cost byproduct propane from shale gas, thereby significantly enhancing the economic efficiency.[1-3] The PDH process is also environmentally sustainable, with carbon emissions of only 2.2 kg-CO_2eq/kg-propylene, which is significantly lower than that from traditional coal-to-propylene routes (16.4 kg-CO_2eq/kg-propylene).[4] However, the PDH reaction is highly endothermic (ΔH = +124 kJ/mol) with an increase in the number of gas molecules, which thermodynamically favors propane conversion at high temperatures or low propane partial pressures.[5] Consequently, the PDH reaction is typically conducted at high temperature of 550–600 °C and atmospheric pressure to achieve significant propane conversion. Since the 1980s, two commercial processes have become the most widely adopted for industrial PDH. One commercial technology is the Oleflex process developed by UOP, which employs a moving-bed reactor with Pt–Sn/Al_2O_3 catalysts.[6] In contrast, the Catofin process, developed by Lummus, utilizes a fixed-bed reactor with Cr_2O_3/Al_2O_3 catalysts.[7] Despite successful industrial implementation, the high temperatures required for PDH accelerate side reactions, leading to low propylene selectivity and coke formation, consequently causing rapid catalyst deactivation.[8-10]

Current catalyst design strategies primarily aim to enhance existing industrial Pt- and Cr-based catalysts.[11] However, as commercial Cr-based catalysts are hindered by toxicity and rapid deactivation,[12] research has shifted toward Pt–M bimetallic catalysts, in which the secondary metal modifies the electronic structure of Pt and improves catalytic performance.[13] For example, Zhao and Gong identified Pt_3In as a promising candidate through systematic screening of Pt–M catalysts, which exhibited only a minor decrease in catalytic activity while significantly improving propylene selectivity.[14] In addition, support optimization represents another strategy to improve catalytic performance, as the support can both stabilize metal dispersion and tune the electronic structure of Pt.[15-18] A notable example from Corma et al. demonstrates that confining PtSn clusters within a K-MFI zeolite enhances metal dispersion, shifts the Pt *d*-band center, and thus achieves high propylene selectivity and long-term stability.[19] Similar strategies have also been reported by Bao and co-workers, with the Pt–Sn@S-1 catalyst achieving long-term stability of up to 4500 h under reaction conditions.[20] Overall, these studies demonstrate that the rational design of both the bimetallic composition and catalyst support can effectively enhance propylene selectivity and suppress coke formation in propane dehydrogenation.

Despite significant achievements, propane dehydrogenation

remains a key challenge due to the intrinsic trade-off between activity and selectivity.[14, 21, 22] Specifically, lowering the C–H activation barrier to enhance activity inevitably strengthens propylene adsorption, which leads to undesired deep dehydrogenation and ultimately coke formation.[23] Therefore, simultaneously improving activity and selectivity on Pt-based catalysts remains challenging. To break this scaling relationship, a Pt/Cu single-atom alloy catalyst has been explored as a promising strategy.[24] Isolated Pt single atoms dispersed in Cu promote propane dehydrogenation and suppress the further dehydrogenation of propylene to the C_3H_5* intermediate. The suppression occurs because a single Pt atom provides only a single adsorption site, preventing multiple Pt–C bonds on Pt surfaces from stabilizing the C_3H_5* intermediate. However, single-atom catalysts inevitably aggregate as isolated metal atoms migrate and coalesce under high-temperature conditions, which underscores the urgent need for alternative types of catalysts.[25, 26]

Ga-based catalysts have attracted considerable attention for PDH due to their remarkable selectivity and stability.[27-30] Among these Ga-based systems, gallium nitride (GaN) has emerged as a promising candidate for PDH with propylene selectivity up to 90%.[31-33] A notable feature of the GaN surfaces found in our previous work is the presence of frustrated Lewis pairs (FLPs),[34-37] which are characterized by the proximity of Lewis acid and Lewis base sites that do not form a chemical bond. Solid FLPs on GaN possess frontier orbitals that are in close proximity, enabling cooperation between the Lewis acid and Lewis base sites for C–H bond activation.[34, 35] However, the detailed mechanisms underlying the specific roles and synergistic interactions of different active sites throughout the entire catalytic cycle remain unexplored. Herein, we report that the cooperation between frustrated Ga···N and Ga···Ga pairs on GaN surfaces can break the intrinsic linear scaling relationship. The Ga···N FLP efficiently promotes the rate-limiting cleavage of the first C–H bond, with a Gibbs free energy of activation of 1.63 eV, slightly lower than that of the industrial Pt_3Sn catalyst. Importantly, the frustrated Ga···Ga pair is identified as the active site for the dehydrogenation of 1-propyl to propylene, exhibiting weak propylene adsorption and suppressing the transformation of the coke precursor C_3H_5*. Furthermore, kinetic Monte Carlo simulations based on the constructed reaction network show a turnover frequency of 18.33 s^{-1} for propylene production, demonstrating outstanding catalytic performance for propane dehydrogenation.

2 Results and Discussion

The GaN(100) surface was chosen to investigate the PDH reaction because of its low surface energy and high catalytic performance.[38, 39] Bader analysis shows that surface Ga carries a positive charge of 1.46 |*e*|, whereas surface N carries a negative charge of –1.48 |*e*| (Figure 1a), indicating that Ga and N atoms can function as Lewis acid and Lewis base sites, respectively. The adsorption energies of probe molecules on Ga and N sites were calculated to further evaluate the intrinsic reactivity. PCl_3 preferentially adsorbs on Ga sites with an adsorption energy of –0.92 eV, whereas Cl_2 binds to N sites with an adsorption energy of –1.08 eV (Figure 1b). The individual acid and base sites further combine into distinct Lewis pairs.[34, 36, 37] Specifically, surface Ga and neighboring N atoms can form classical Lewis pairs (CLPs) characterized by short bonds (1.78 Å, as shown in Figure 1a). COHP analysis of the Ga–N bonds reveals significant bonding states below the Fermi level (Figure 1c), which is consistent with the thermal stability of GaN reported in the literature.[40, 41] In contrast, Ga atoms can also combine with next-neighboring N atoms to form FLPs with a longer acid–base distance of 3.33 Å (Figure 1a). Beyond these acid-base pairs, adjacent Ga···Ga pairs with a distance of 3.12 Å are termed frustrated metal pairs and are considered potential active sites (Figure 1a). Previous studies have identified FLPs as the dominant active sites due to their higher activity over CLPs,[34] whereas the catalytic potential of Ga···Ga pairs has received less attention.

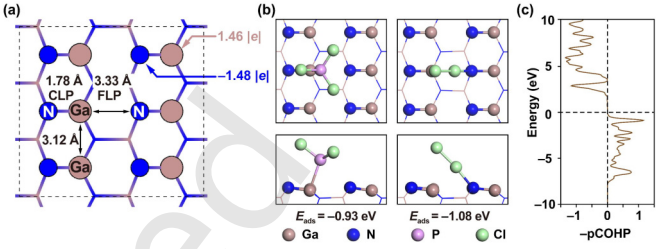

Figure 1. Structural and electronic properties of active sites on GaN(100). (a) Atomic structure and charge distribution of the GaN(100) surface. (b) The adsorption energies probe molecule on Ga and N sites. (c) COHP analysis of the surface Ga–N bond.

2.1 Breaking the Linear Scaling Relationship over GaN Surface

A detailed analysis of propane dehydrogenation was conducted to understand the roles of different active sites on the GaN surface.

Propane can dissociate at the Ga···N FLPs with a G_a of 1.63 eV to produce 1-propyl (Figure 2a) and a ΔG of 0.53 eV (Figure 2c). Notably, the G_a value for propane dissociation to 2-propyl is higher (1.71 eV, shown in Figure S1). In contrast, propane dissociation at the frustrated Ga···Ga pair is thermodynamically highly unfavorable (ΔG = 3.01 eV). A comparison with the CLPs shows a significantly higher activation energy for C–H bond cleavage than the corresponding value on FLPs (Figure S2), indicating the Ga···N FLPs serve as the active site for propane dissociation. As a reference, $Pt_3Sn(111)$ was used as a model for Pt–Sn catalysts due to its widespread use in computational PDH studies and well-defined surface structure. The Pt–Sn system is well-characterized and industrially relevant, providing a commonly used benchmark for evaluating new catalysts.[42, 43] The G_a for propane dissociation on $Pt_3Sn(111)$ is 1.82 eV (Figure S1), slightly higher than that on GaN. The rate constants are calculated to be 5.66×10^2 s^{-1} for $Pt_3Sn(111)$ and 7.08×10^3 s^{-1} for GaN at 873 K, indicating superior activity of GaN, consistent with the excellent C–H bond activation performance reported experimentally for GaN.[44, 45]

The second C–H dissociation on Ga···N FLPs is both kinetically and thermodynamically unfavorable (G_a = 1.43 eV, ΔG = 0.93 eV, Figure S3). In contrast, the frustrated Ga···Ga pair facilitates this step with much lower Gibbs free energies of activation and reaction (G_a = 0.92 eV, ΔG = 0.58 eV). In summary, the first C–H activation of propane to 1-propyl possesses the higher intrinsic barrier, identifying it as the rate-determining step for the PDH reaction. Overall, propane dehydrogenation occurs at the Ga···N FLP site, while dehydrogenation of the 1-propyl intermediate proceeds at the frustrated Ga···Ga pair.

Adsorption energies (E_{ads}) directly reflect the intrinsic molecule–surface binding strength, as they avoid the significant

errors caused by entropic contributions present in Gibbs free energies, especially for weakly adsorbed molecules. Importantly, the adsorption of propylene is weaker on GaN (–0.79 eV) than on Pt_3Sn (–1.08 eV, Figure S1). Moreover, the Ga–C distance increases from 1.98 Å to 2.66 Å during the dissociation of 1-propyl to propylene on the frustrated Ga···Ga pair (Figure 2c), indicating that the Ga–C bond is broken and propylene is physically adsorbed on the surface. In contrast, propylene is chemically adsorbed on the Pt site of $Pt_3Sn(111)$, with two Pt–C bond lengths of 2.22 Å and 2.28 Å (Figure 2d). Overall, weak propylene adsorption is facilitated by frustrated Ga···Ga pairs, enabling GaN to outperform Pt_3Sn in propylene desorption.

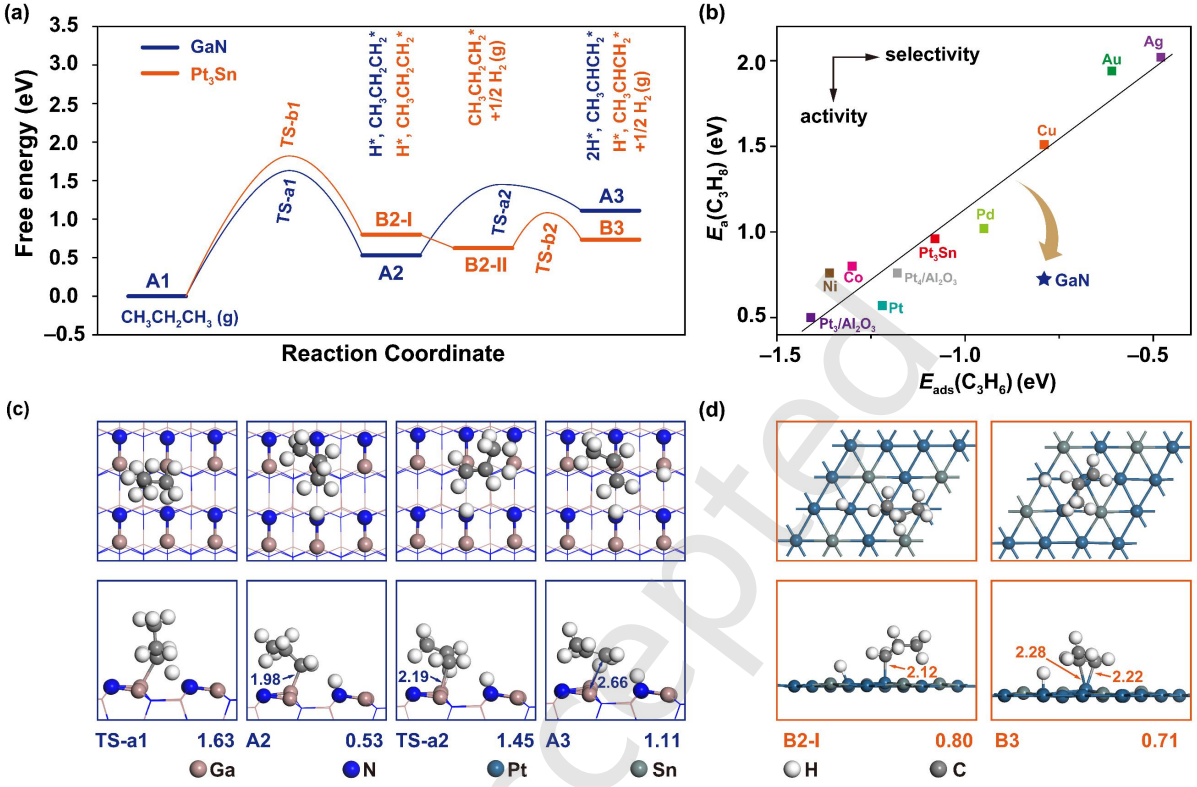

Figure 2. (a) Free energy profile for propane dehydrogenation at 873 K. The zero-point energy reference corresponds to the sum of Gibbs free energies of gas-phase propane and the clean surfaces. (b) Linear relationship between the activation energy of the first C–H bond cleavage and adsorption energy of propylene. The energy data of Pd, Pt, Pt_n/Al_2O_3 (n = 3 and 4) are cited from previous studies.[46-48] Optimized structures of the intermediates and transition states on (c) GaN(100) and (d) $Pt_3Sn(111)$ surfaces. The numbers below the frames represent Gibbs free energies in eV, and the numbers inside the frames represent distances in Å.

To benchmark the catalytic performance of GaN among other catalysts, we established a linear scaling relationship between the activation energy for the first C–H bond cleavage in propane and the adsorption energy of propylene (Figure 2b). The first C–H bond activation of propane is the rate-determining step for the PDH reaction (Figure 2a), with its activation energy serving as an activity descriptor, while the adsorption energy of propylene is related to product selectivity and thus functions as a selectivity descriptor. As shown in Figure 2b, the scaling relationship shows that catalysts with weaker propylene adsorption generally exhibit higher activation energy for propane dissociation, indicating the inherent activity-selectivity trade-off. However, on GaN, the low activation energy of the first dehydrogenation step at Ga···N FLPs enables high activity comparable to Ni and Co, while propylene adsorption is significantly weaker than on these metals. Overall, these findings demonstrate that GaN can simultaneously achieve high activity and weak propylene adsorption, thus overcoming the intrinsic scaling relationship of traditional catalysts. These results indicate that the construction of neighboring dual active sites with distinct electronic properties could be an effective strategy to circumvent the linear scaling relationships.

2.2 Mechanistic Insights into Breaking Scaling Relationship

To further elucidate the mechanism by which FLPs and Ga···Ga pairs break the linear scaling relationship on GaN, a detailed mechanistic investigation of propane dehydrogenation was conducted. To clarify the role of frustrated Ga···N and Ga···Ga pairs in C–H activation, a combination of electronic structure analyses and constrained *ab initio* molecular dynamics (AIMD) simulations was performed to investigate their interactions with propane. The charge density difference reveals electron accumulation between Ga and C accompanied by electron depletion around H (Figure 3a), which is indicative of heterolytic C–H bond cleavage of propane at the FLPs. Notably, the ELF map in Figure 3b exhibits a region with values exceeding 0.5 between C, H, and N atoms, indicating covalent interactions in both C–H and N–H bonds. Projected density of states (PDOS) analysis reveals pronounced peaks for both propane and the N site at –1.2 eV (Figure 3c), suggesting orbital overlap and electron transfer from the N 2*p* orbitals to the antibonding orbitals of the C–H bonds in propane. Meanwhile, a back-donation of electrons from the bonding orbitals of propane to the unoccupied states of the Lewis acid (Ga) site is observed at –3.6 eV, revealing a cooperation between Lewis acid and Lewis base sites within FLP for the first C–H bond activation of propane.

Constrained AIMD simulations were performed to elucidate

the roles of its Lewis acid and base sites on the first C–H bond activation of propane. As shown in Figures 3d and 3e, propane initially adsorbs at the Ga site, with the Ga···C distance decreasing from approximately 3.5 Å to around 2 Å. Subsequently, while the Ga···C distance remains nearly constant, the N···H distance decreases from 2.5–3.5 Å to approximately 1 Å, corresponding to the C–H bond cleavage and the N–H bond formation. These results indicate that the Ga site is primarily responsible for propane adsorption, whereas the strongly basic N site facilitates C–H bond activation by donating electrons to the antibonding orbital of the C–H bond.

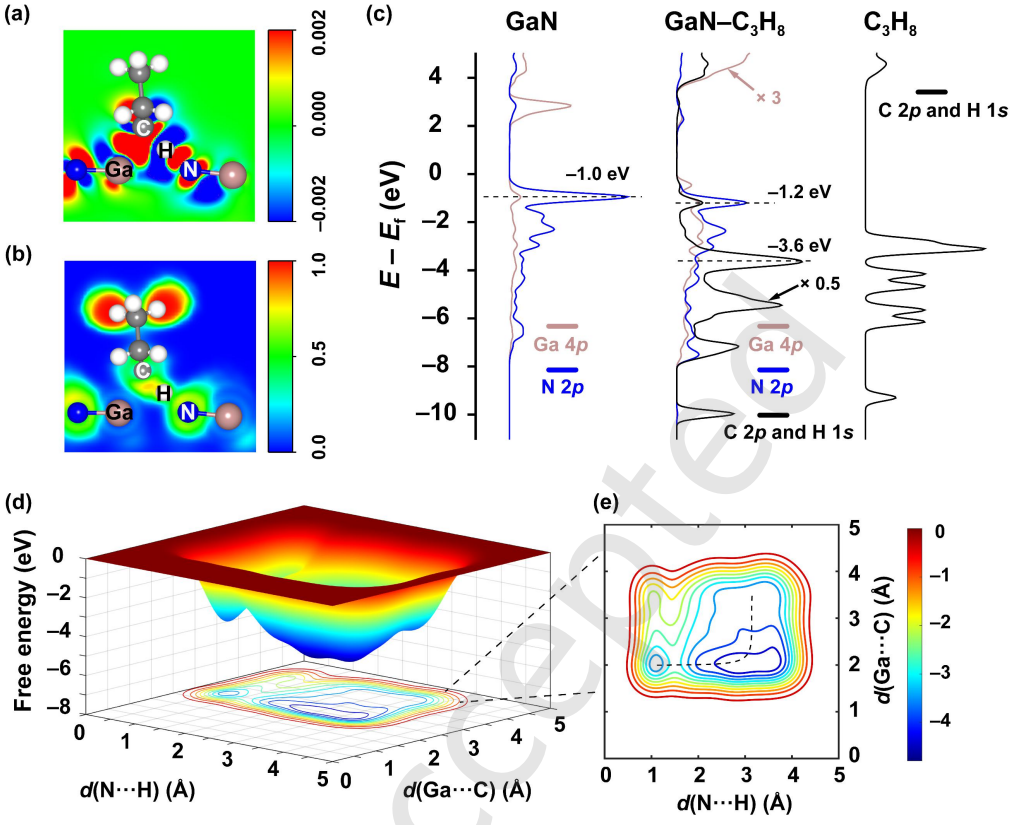

Figure 3. (a) Charge density difference ($\Delta\rho = \rho(\mathrm{TS}) - \rho(\mathrm{surface}^{\#}) - \rho(\mathrm{C_3H_8}^{\#})$) map, (b) ELF map, and (c) PDOS analysis at the TS for propane dehydrogenation. The (d) 3D and (e) 2D free energy profiles as functions of the controlled variables of d(N···H) and d(Ga···C).

As another key step in propane dissociation, 1-propyl dehydrogenation was analyzed to elucidate the role of the frustrated Ga···Ga pair. The charge density difference map in Figure 4a reveals a significant increase in electron density around the H_I atom, accompanied by depletion around the C_{II} atom, indicating partial electron transfer from the carbon to the hydrogen. The ELF map shows values between 0.5 and 1.0 around H_I (Figure 4b), suggesting that the hydrogen atom gains electrons and forms a hydride species on the Ga_{II} site. The Ga_{II} site, possessing empty 4*p* orbitals (Figure 3c), acts as an electron acceptor, while the adjacent Ga_I site also gains electron density from the 1-propyl intermediate (Figure 4a), highlighting the cooperative role of the Ga···Ga pair in facilitating this dehydrogenation step. A more detailed investigation of the 1-propyl dehydrogenation process was conducted using constrained AIMD simulations (Figure 4, c and d). The local minimum in the upper-left region of the potential energy surface corresponds to 1-propyl adsorption at the Ga_I site, with the Ga_I–C_I bond maintained at approximately 2 Å and the Ga_{II}···H_I distance ranging from 2 to 3 Å (Figure 4, c and d). Along the reaction coordinate, the Ga_I–C_I bond gradually elongates to 2.5–3.0 Å, which can be regarded as indicative of bond cleavage. Subsequently, the Ga_{II}···H_I distance decreases from 2.0–2.5 Å to about 1.6 Å, indicating the formation of a Ga–H bond. Overall, our calculations show that the N site within FLPs facilitates the rate-limiting cleavage of the first C–H bond whereas the Ga···Ga pair governs propylene adsorption, thereby revealing how GaN simultaneously achieves high C–H activation capability and weak propylene adsorption.

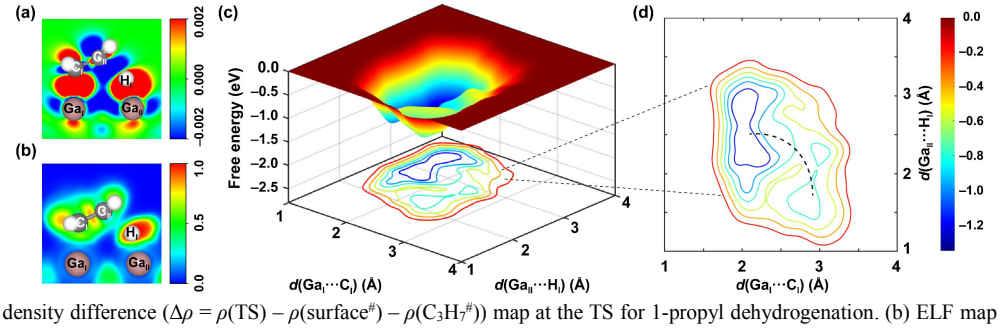

Figure 4. (a) Charge density difference ($\Delta\rho = \rho(\mathrm{TS}) - \rho(\mathrm{surface}^{\#}) - \rho(\mathrm{C_3H_7}^{\#})$) map at the TS for 1-propyl dehydrogenation. (b) ELF map at the TS for 1-propyl dehydrogenation. The (c) 3D and (d) 2D free energy profiles as functions of the controlled variables of d(Ga_I···C_I) and d(Ga_{II}···H_I).

As discussed above, propylene is physically adsorbed at the Ga site of GaN, whereas it binds chemically to the Pt_3Sn surface (Figure 2). To further elucidate the origin of this difference, the electronic interactions were analyzed through charge density difference, ELF, and PDOS calculations. As shown in Figure 5a, charge density difference indicates that the electron density around the propylene molecule decreases, while the Ga atom gains electrons, suggesting the π electrons of propylene transfer to the empty orbitals of Ga^{3+}. Furthermore, the ELF analysis reveals a negligible electron localization between the Ga atom and the C atoms of propylene, consistent with physical adsorption of propylene at the Ga site. In good agreement with the ELF map, the PDOS shows only a few overlaps between propylene and the Ga 4*p* orbitals, indicating that their interaction is dominated by weak electronic coupling (Figure 5c). In contrast, the charge density difference indicates an accumulation of electron density on the π* antibonding orbitals of propylene, accompanied by a depletion of electron density around the Pt atoms (Figure 5b). PDOS analysis exhibits significant orbital overlap between propylene and the Pt 5d_{yz} orbitals (Figures 5d and S4), further confirming the strong electronic interaction between Pt and propylene. In summary, the electron-rich Pt in Pt_3Sn catalysts enables the donation of electrons to the π* antibonding orbitals of propylene, leading to strong adsorption of propylene. In contrast, the adsorption of propylene on the Ga site is dominated by van der Waals interactions, with only a few electron transfers from its π orbitals to the empty Ga 4*p* orbitals (Figure 5, e and f).

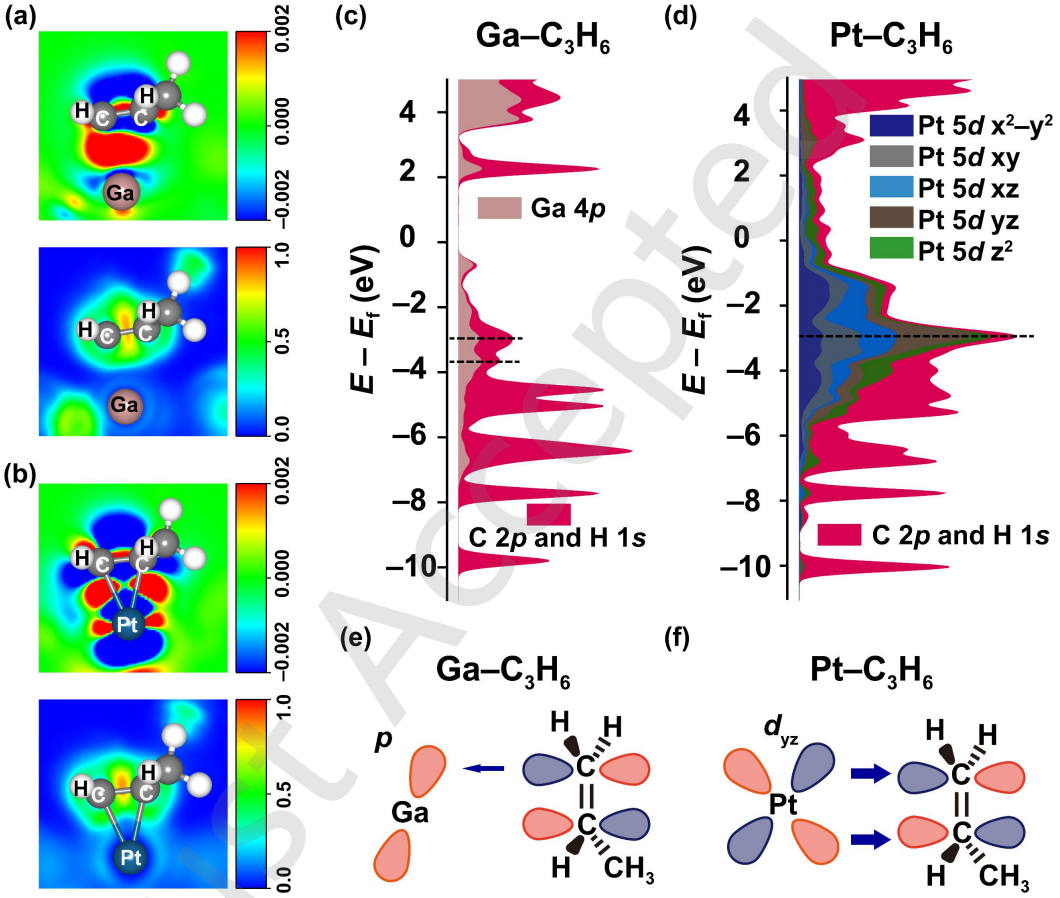

Figure 5. Analysis of propylene adsorption on GaN(100) and Pt_3Sn(111) surfaces. Electron density difference ($\Delta\rho = \rho(surface\_C_3H_6^{\#}) - \rho(surface^{\#}) - \rho(C_3H_6^{\#})$) map and their corresponding electron localization function map for propylene adsorption on (a) GaN(100) and (b) Pt_3Sn(111). Projected density of states of C_3H_6 and its adsorption sites on (c) GaN(100) and (d) Pt_3Sn(111). Interaction modes between C_3H_6 and active sites on (e) GaN(100) and (f) Pt_3Sn(111).

2.3 Coke-resistance Analysis

The deep dehydrogenation of propylene on GaN(100) was investigated to elucidate the coke-resistance ability of GaN, with Pt_3Sn(111) serving as a reference for comparison. At 873 K, propylene desorption into the gas phase is thermodynamically favorable on both GaN(100) and Pt_3Sn(111), with Gibbs free energies of desorption of –1.30 eV and –1.08 eV (Figure 6, a and c), respectively. By comparison, propylene dehydrogenation to form C_3H_5* (*i.e.*, $CH_3C{=}CH_2$*) is much less favorable than propylene desorption. Although only a small fraction of propylene undergoes dehydrogenation, the resulting $CH_3C{=}CH_2$* intermediate is critical, as it is a key coke precursor.[20, 49, 50] On GaN, further dehydrogenation of $CH_3C{=}CH_2$* requires a kinetic barrier as high as 1.92 eV, whereas hydrogenation to regenerate propylene requires only 1.01 eV. The rate constant for $CH_3C{=}CH_2$* hydrogenation to $CH_3CH{=}CH_2$* reaches 2.69×10^7 s^{-1}, whereas dehydrogenation proceeds at 1.50×10^2 s^{-1}, roughly five orders of magnitude lower than the hydrogenation rate. In contrast, on the Pt_3Sn(111) surface, the barrier for further dehydrogenation of $CH_3C{=}CH_2$* is only 0.58 eV, 0.29 eV lower than that for hydrogenation to regenerate propylene. The rate constants are 8.16×10^9 s^{-1} for dehydrogenation and 1.7×10^8 s^{-1} for hydrogenation to $CH_3CH{=}CH_2$*, corresponding to a rate-constant ratio of dehydrogenation to hydrogenation of 47 on Pt_3Sn(111). To elucidate the origin of the distinct catalytic performance, the adsorption configurations of $CH_3C{=}CH_2$* on both GaN(100) and Pt_3Sn(111) surfaces were analyzed. On GaN, $CH_3C{=}CH_2$* adopts a σ-bonded adsorption configuration with a

C=C bond length of 1.34 Å (Figure 6b). In contrast, on $Pt_3Sn(111)$, the $CH_3C=CH_2$* intermediate forms three Pt–C bonds with the surface, and its C=C bond is significantly elongated to 1.48 Å (Figure 6d). Charge density difference analysis shows electron donation from Pt to the π* orbitals of $CH_3C=CH_2$*, resulting in substantial activation of the adsorbed intermediate. Overall, the high barrier for deep dehydrogenation of the coke precursor $CH_3C=CH_2$* on GaN contributes to coke resistance and product selectivity.

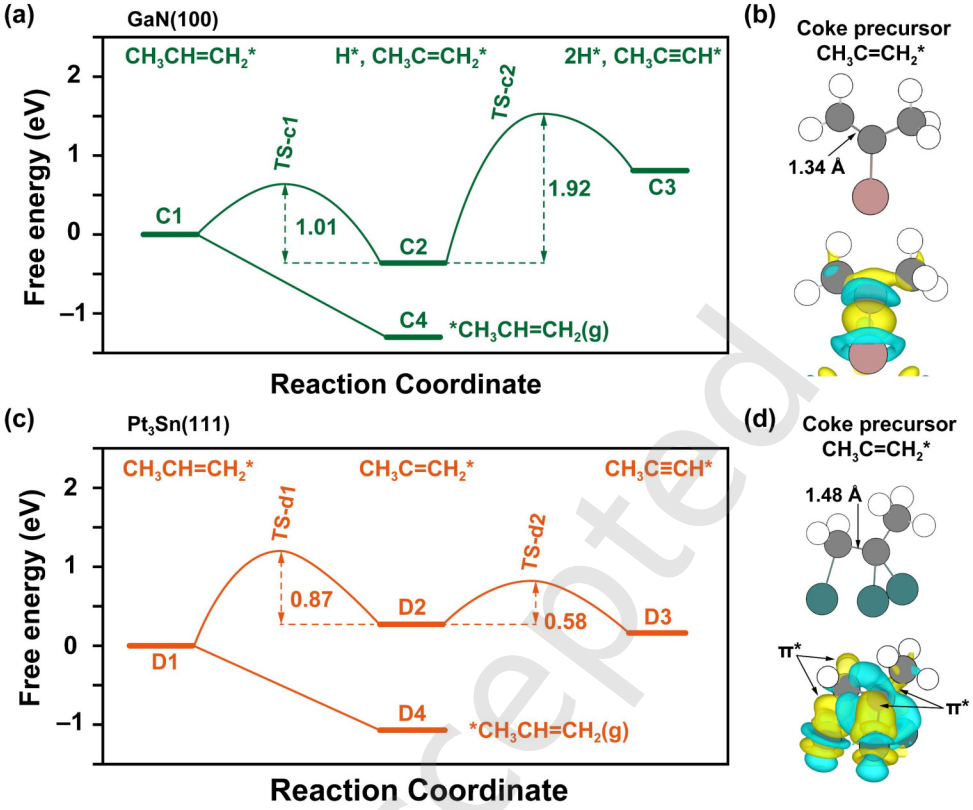

Figure 6. Potential energy surfaces for propylene desorption and dehydrogenation on (a) GaN(100) and (c) $Pt_3Sn(111)$. The zero of the energy scale is referenced to the energy of a propylene molecule adsorbed on the surface. Adsorption configurations and charge density difference maps of the $CH_3C=CH_2$* intermediate on (b) GaN(100) and (d) $Pt_3Sn(111)$. The iso-surface of the charge density difference maps are plotted at a contour value of 0.003 *e*/Bohr^3.

2.4 Reaction Network and Microkinetic for PDH over GaN

Apart from the direct dehydrogenation of propane to propylene, a series of side reactions was computed to construct the overall reaction network, as illustrated in Figure 7. These side reactions can be classified into three major categories. The first class involves stepwise dehydrogenation of C_3H_x* intermediates. For instance, 1-propyl and 2-propyl intermediates can undergo further dehydrogenation to form $CHCH_2CH_3$* and CH_3CCH_3*. The corresponding G_a values are 1.49 eV and 1.41 eV, with ΔG of 1.24 eV and 0.90 eV (Figures S5–S6), indicating that these pathways are thermodynamically and kinetically unfavorable under reaction conditions. Collectively, the G_a values for deep dehydrogenation of C_3H_x* intermediates are 0.42 eV for CH_3CH_2CH*, 1.60 eV for $CH_3CH=CH$*, and 1.92 eV for $CH_3C=CH_2$* (Figure 7b), suggesting that some of the deep dehydrogenation steps are kinetically hindered. The second class comprises C–C bond cleavage of C_3H_x* intermediates, producing C1 and C2 fragments. The kinetic barriers for C–C bond dissociation of the four C_3H_x* intermediates, CH_3CH_2CH*, $CH_3CH=CH$*, CH_3CCH_3*, and $CH_3C=CH_2$*, are 1.84, 2.52, 1.90, and 2.57 eV, respectively, all higher than the activation energies of their dehydrogenation steps. The third class includes further dehydrogenation of the C1 and C2 fragments, which may ultimately contribute to coke formation. As for the CH_3* dissociation pathways, formation of CH_2*, CH*, and C* requires activation barriers of 3.01, 2.47, and 1.71 eV, respectively. For the C_2 species, the highest barrier along the C_2H_4* dehydrogenation pathway to C≡C* is 4.16 eV. In summary, a comprehensive reaction network containing 37 elementary steps (Tables S1–S4) was constructed by incorporating these pathways, along with H_2 desorption and intermediate migration.

Following the construction of a comprehensive reaction network for propane dehydrogenation, a microkinetic model was built based on the energetic parameters of all elementary steps. The temperature was set at 873 K with a propane partial pressure of 1 bar. As illustrated in Figure 8a, propylene formation on the GaN surface occurs predominantly via the 1-propyl pathway, which accounts for 98.265% of the total propylene yield. In contrast, the 2-propyl pathway contributes to only 1.735% of the total propylene yield. These results originate from the DFT-based energetic parameters: the G_a values for propane to propylene through the 1-propyl pathway are lower than those for the 2-propyl pathway (Figures 2 and S1). It was found that the $CHCH_2CH_3$* and CH_3CCH_3* intermediates were not observed, which is attributed to the kinetic and thermodynamic unfavourability for the 1-propyl and 2-propyl dehydrogenation (Figure 7). In good agreement with the facile propylene desorption and hindered $CH_3CH=CH$* transformation (Figure 6), microkinetic analysis reveals that 99.997% of the surface propylene desorbs into the gas phase. A trace amount (0.003%) of propylene converts to $CH_3CH=CH$*, which does not proceed to further reaction, thus effectively preventing coke formation. The kMC simulation further demonstrates that the turnover frequency of propylene production can reach up to

18.33 s^{-1} (Figure 8b), significantly higher than that of conventional Pt-based and Cr-based catalysts.[51, 52] Overall, the microkinetic simulations confirm the superior catalytic performance of GaN, characterized by a high TOF and excellent resistance to coking.

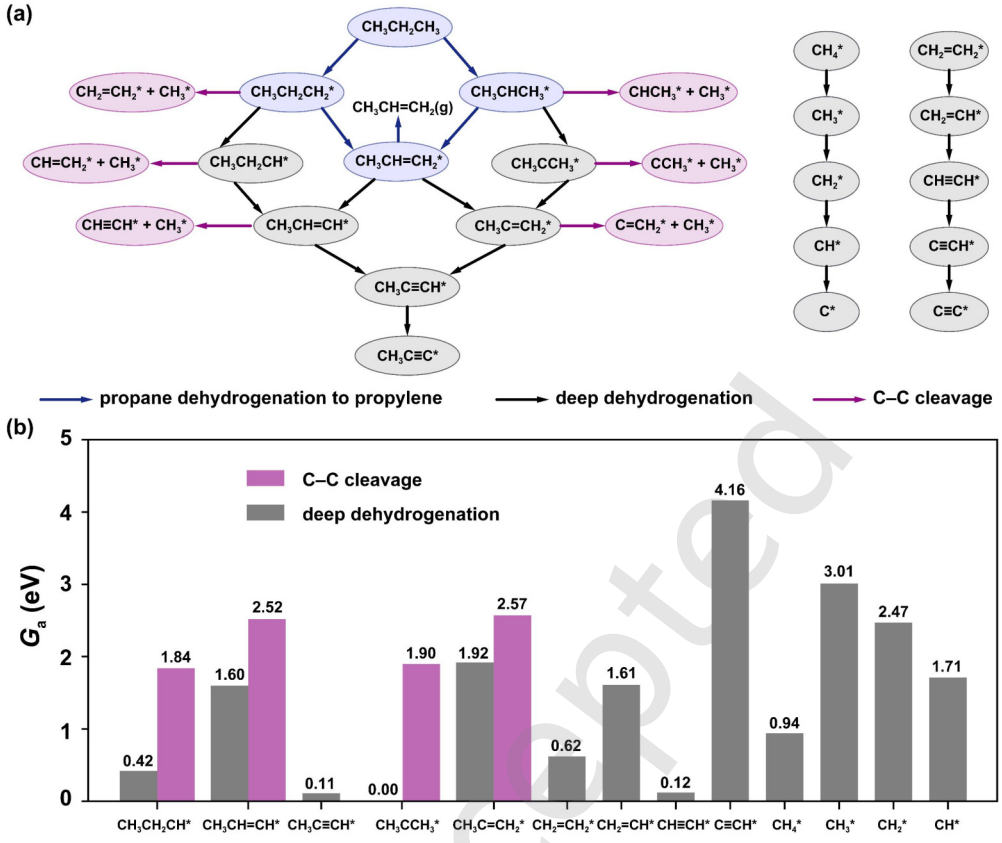

Figure 7. (a) Reaction network of propane dehydrogenation for microkinetic modeling. (b) G_a values for dehydrogenation and C–C bond cleavage. The optimized structures are shown in Figures S7–S8.

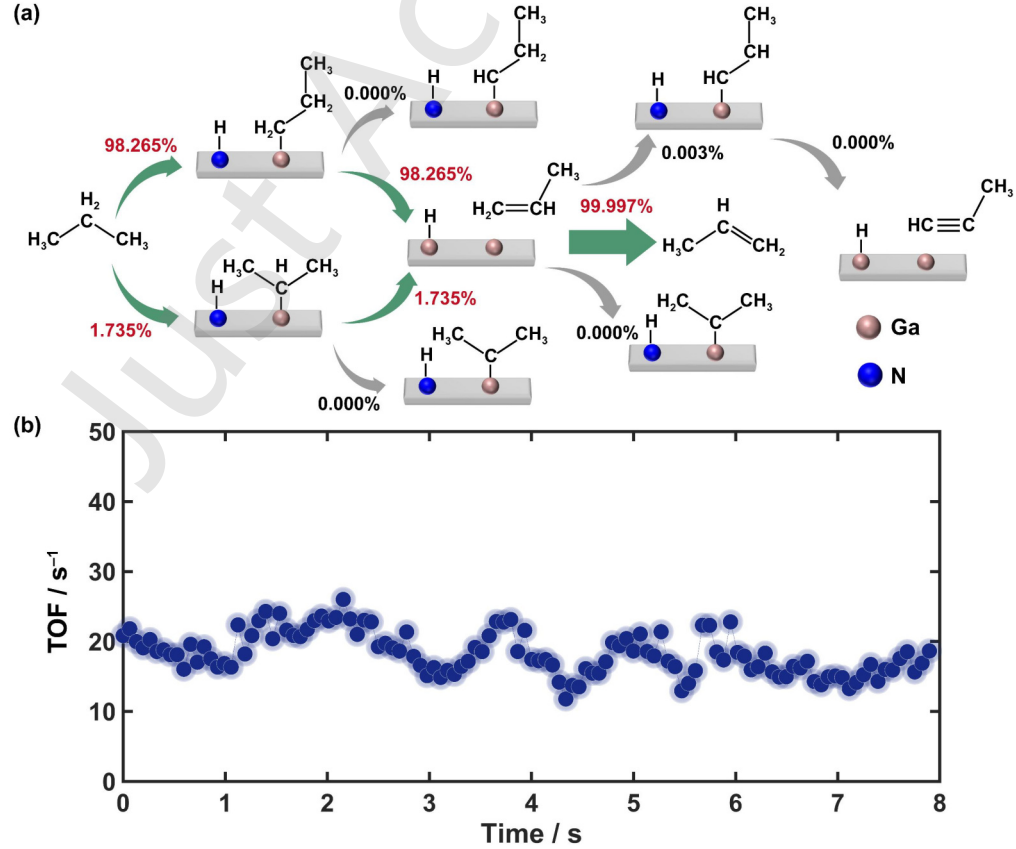

Figure 8. (a) Flux calculation for propane dehydrogenation at 873 K over the GaN(100) surface. (b) Time-dependent evolution of turnover frequency for propylene production.

3. Conclusion

In conclusion, this work demonstrates that the cooperation of

frustrated Ga···N and Ga···Ga pairs on GaN surfaces breaks the inherent linear scaling relationship of propane dehydrogenation, enabling high activity and propylene selectivity simultaneously. The rate-limiting step, propane dissociation to 1-propyl, is promoted by the frustrated Ga···N Lewis pairs with a Gibbs free energy barrier of 1.63 eV, lower than that on Pt_3Sn. The frustrated Ga···Ga metal pairs are responsible for 1-propyl dehydrogenation and ensure the facile desorption of propylene. The high barrier (1.92 eV) for coke formation demonstrates the remarkable coke-resistance ability of GaN. Kinetic Monte Carlo simulations based on the constructed reaction network confirm the excellent performance of GaN, with a turnover frequency of 18.33 s^{-1} for propylene production. These results uncover the role of frustrated Ga···N and Ga···Ga pairs in breaking the scaling relationship and provide insights for designing more efficient catalysts for propane dehydrogenation.

Electronic Supplementary Material: Supplementary material (please provide the brief detail of the ESM) is available in the online version of this article at https://doi.org/10.26599/NR.2026.94908714.

Data availability

All data needed to support the conclusions in the paper are presented in the manuscript and/or the Electronic Supplementary Material. Additional data related to this paper may be requested from the corresponding author upon request.

Acknowledgements

This work is financially supported by the National Key R&D Program of China (No. 2023YFA1506302), the National Natural Science Foundation of China (No. U23A20112), the S&T Program of Energy Shaanxi Laboratory (No. ESLB202404), the Shaanxi Provincial Research and Development Platform for Generic Technologies (No. 2025ZY1-GXJS-03), the Fundamental Research Funds for the Central Universities (No. xtr052025020), and the CAS-Yulin University Joint Fund (YLU-DNL Fund2025008). C. R. C. acknowledges the Shaanxi Technological Innovation Team (No. 2024RS-CXTD-47), the CAS Youth Interdisciplinary Team, and the NSFC Center for Single-Atom Catalysis (No. 22388102).

Declaration of competing interest

All the contributing authors report no conflict of interests in this work.

Author contribution statement

Xi-Yang Yu: Data curation, Formal analysis, Investigation, Methodology, Visualization, Writing – original draft. Han-Xuan Liu: Formal analysis. Han-Tao Cheng: Investigation. Zheng-Qing Huang: Formal analysis, Writing – review & editing. Chun-Ran Chang: Conceptualization, Funding acquisition, Project administration, Resources, Supervision, Writing – review & editing. All the authors have approved the final manuscript.

Use of AI statement

None.

References

[1] Yang, M.; You, F. Comparative Techno-Economic and Environmental Analysis of Ethylene and Propylene Manufacturing from Wet Shale Gas and Naphtha. *Ind. Eng. Chem. Res.* **2017**, *56*, 4038–4051.
[2] Song, S.; Sun, Y.; Yang, K.; Fo, Y.; Ji, X.; Su, H.; Li, Z.; Xu, C.; Huang, G.; Liu, J.; Song, W. Recent Progress in Metal-Molecular Sieve Catalysts for Propane Dehydrogenation. *ACS Catal.* **2023**, *13*, 6044–6067.
[3] Otroshchenko, T.; Jiang, G.; Kondratenko, V. A.; Rodemerck, U.; Kondratenko, E. V. Current Status and Perspectives in Oxidative, Non-Oxidative and CO_2-Mediated Dehydrogenation of Propane and Isobutane over Metal Oxide Catalysts. *Chem. Soc. Rev.* **2021**, *50*, 473–527.
[4] Rodríguez-Vallejo, D. F.; Guillén-Gosálbez, G.; Chachuat, B. What Is the True Cost of Producing Propylene from Methanol? The Role of Externalities. *ACS Sustain. Chem. Eng.* **2020**, *8*, 3072-3081.
[5] Chen, S.; Chang, X.; Sun, G.; Zhang, T.; Xu, Y.; Wang, Y.; Pei, C.; Gong, J. Propane Dehydrogenation: Catalyst Development, New Chemistry, and Emerging Technologies. *Chem. Soc. Rev.* **2021**, *50*, 3315–3354.
[6] Monai, M.; Gambino, M.; Wannakao, S.; Weckhuysen, B. M. Propane to Olefins Tandem Catalysis: A Selective Route Towards Light Olefins Production. *Chem. Soc. Rev.* **2021**, *50*, 11503–11529.
[7] Sattler, J. J. H. B.; Ruiz-Martinez, J.; Santillan-Jimenez, E.; Weckhuysen, B. M. Catalytic Dehydrogenation of Light Alkanes on Metals and Metal Oxides. *Chem. Rev.* **2014**, *114*, 10613-10653.
[8] Li, Q.; Sui, Z.; Zhou, X.; Zhu, Y.; Zhou, J.; Chen, D. Coke Formation on Pt–Sn/Al_2O_3 Catalyst in Propane Dehydrogenation: Coke Characterization and Kinetic Study. *Top. Catal.* **2011**, *54*, 888–896.
[9] Lian, Z.; Ali, S.; Liu, T.; Si, C.; Li, B.; Su, D. S. Revealing the Janus Character of the Coke Precursor in the Propane Direct Dehydrogenation on Pt Catalysts from a kMC Simulation. *ACS Catal.* **2018**, *8*, 4694–4704.
[10] He, Z.; Yang, J.; Liu, L. Design of Supported Metal Catalysts and Systems for Propane Dehydrogenation. *JACS Au* **2024**, *4*, 4084–4109.
[11] Hu, Z.-P.; Yang, D.; Wang, Z.; Yuan, Z.-Y. State-of-the-Art Catalysts for Direct Dehydrogenation of Propane to Propylene. *Chin. J. Catal.* **2019**, *40*, 1233–1254.
[12] Carter, J. H.; Bere, T.; Pitchers, J. R.; Hewes, D. G.; Vandegehuchte, B. D.; Kiely, C. J.; Taylor, S. H.; Hutchings, G. J. Direct and Oxidative Dehydrogenation of Propane: From Catalyst Design to Industrial Application. *Green Chem.* **2021**, *23*, 9747–9799.
[13] Sun, G.; Luo, R.; Fu, D.; Wu, K.; Wang, X.; Bian, X.; Lu, Z.; Chang, X.; Wang, Z.; Huang, S.; Zhu, Y.; Zhou, J.; Chen, S.; Pei, C.; Zhao, Z. J.; Gong, J. Full Utilization of Noble Metals by Atom Abstraction for Propane Dehydrogenation. *Science* **2025**, *390*, eadw3053.
[14] Zha, S.; Sun, G.; Wu, T.; Zhao, J.; Zhao, Z.-J.; Gong, J. Identification of Pt-Based Catalysts for Propane Dehydrogenation Via a Probability Analysis. *Chem. Sci.* **2018**, *9*, 3925–3931.
[15] Xu, Z.; Yue, Y.; Bao, X.; Xie, Z.; Zhu, H. Propane Dehydrogenation over Pt Clusters Localized at the Sn Single-Site in Zeolite Framework. *ACS Catal.* **2019**, *10*, 818-828.
[16] Shan, Y.; Hu, H.; Fan, X.; Zhao, Z. Recent Progress in Catalytic Dehydrogenation of Propane over Pt-Based Catalysts. *Phys. Chem. Chem. Phys.* **2023**, *25*, 18609–18622.
[17] Valls, M. I.; Ara, J.; Escolastico, S.; Remiro-Buenamanana, S.; Catalan-Martinez, D.; Grand, J.; Kindelmann, M.; Mayer, J.; Somacescu, S.; Curulla-Ferre, D.; Serra, J. M. Redox-Acidity Interplay in Eu-Promoted $PtSn_2$ Catalysts for Selective and Stable Propane Dehydrogenation. *Angew. Chem. Int. Ed.* **2025**, *64*, e202512853.
[18] Liu, H.; Zhang, Y.; Liu, L.; Chen, T.; Zhang, X.; Hu, P.; Xiong, C.; Zhou, J.; Zhang, H.; Dong, L.; Lo, T. W. B.; Nan, B.; He, X.; Ji, H. Platinum Clusters Stabilized by Zincosilicate Zeolite for Efficient Propane Dehydrogenation. *Chin. J. Catal.* **2025**, *71*, 208–219.
[19] Martínez Gómez-Aldaraví, A.; Millán, R.; Millet, I.; Alós, A.; Vidal-Moya, A.; Meyer, R. J.; Martínez, C.; Corma, A.; Boronat, M.; Serna, P.; Moliner, M. Resolving Complex K–Pt–Sn Interactions in PtSn@K-MFI Catalysts for Alkane Dehydrogenation. *J. Am. Chem. Soc.* **2025**, *147*, 12833–12844.
[20] Xu, Z.; Gao, M.; Wei, Y.; Yue, Y.; Bai, Z.; Yuan, P.; Fornasiero, P.; Basset, J. M.; Mei, B.; Liu, Z.; Zhu, H.; Ye, M.; Bao, X. Pt Migration-Lockup in Zeolite for Stable Propane Dehydrogenation Catalyst. *Nature* **2025**, *643*, 691–698.
[21] Chang, X.; Moskaleva, L.; Zhao, Z.-J.; Gong, J. Activity-Selectivity Trade-Off in Propane Dehydrogenation: Pt–C Repulsion Is the Essence. *J. Phys. Chem. C* **2024**, *128*, 12931–12937.
[22] Xiao, L.; Ma, F.; Zhu, Y.-A.; Sui, Z.-J.; Zhou, J.-H.; Zhou, X.-G.; Chen, D.; Yuan, W.-K. Improved Selectivity and Coke Resistance of Core-Shell Alloy Catalysts for Propane Dehydrogenation from First Principles and Microkinetic Analysis. *Chem. Eng. J.* **2019**, *377*, 120049.
[23] Chang, X.; Lu, Z.; Luo, R.; Wang, X.; Sun, G.; Fu, D.; Zhao, Z.-J.; Gong, J. Microenvironment Engineering of Non-Noble Metal Alloy for Selective Propane Dehydrogenation. *Chem* **2025**, *11*, 102294.
[24] Sun, G.; Zhao, Z.-J.; Mu, R.; Zha, S.; Li, L.; Chen, S.; Zang, K.; Luo, J.; Li, Z.; Purdy, S. C.; Kropf, A. J.; Miller, J. T.; Zeng, L.; Gong, J.

Breaking the Scaling Relationship Via Thermally Stable Pt/Cu Single Atom Alloys for Catalytic Dehydrogenation. *Nat. Commun.* **2018**, *9*, 4454.
[25] Liu, J.-C.; Tang, Y.; Wang, Y.-G.; Zhang, T.; Li, J. Theoretical Understanding of the Stability of Single-Atom Catalysts. *Natl. Sci. Rev.* **2018**, *5*, 638–641.
[26] Su, Y.-Q.; Zhang, L.; Wang, Y.; Liu, J.-X.; Muravev, V.; Alexopoulos, K.; Filot, I. A. W.; Vlachos, D. G.; Hensen, E. J. M. Stability of Heterogeneous Single-Atom Catalysts: A Scaling Law Mapping Thermodynamics to Kinetics. *Npj Comput. Mater.* **2020**, *6*, 144.
[27] Searles, K.; Chan, K. W.; Mendes Burak, J. A.; Zemlyanov, D.; Safonova, O.; Copéret, C. Highly Productive Propane Dehydrogenation Catalyst Using Silica-Supported Ga–Pt Nanoparticles Generated from Single-Sites. *J. Am. Chem. Soc.* **2018**, *140*, 11674–11679.
[28] Castro-Fernández, P.; Mance, D.; Liu, C.; Moroz, I. B.; Abdala, P. M.; Pidko, E. A.; Copéret, C.; Fedorov, A.; Müller, C. R. Propane Dehydrogenation on Ga_2O_3-Based Catalysts: Contrasting Performance with Coordination Environment and Acidity of Surface Sites. *ACS Catal.* **2021**, *11*, 907–924.
[29] Yuan, Y.; Lee, J. S.; Lobo, R. F. Ga^+-Chabazite Zeolite: A Highly Selective Catalyst for Nonoxidative Propane Dehydrogenation. *J. Am. Chem. Soc.* **2022**, *144*, 15079–15092.
[30] Zhao, Z.; Zhong, Y.; Chang, X.; Xu, B. C–H Bond Activation of Propane on $Ga_2O_2^{2+}$ in Ga/H-ZSM-5 and Its Mechanistic Implications. *Chin. J. Catal.* **2024**, *64*, 32–43.
[31] Zhu, Z.-J.; He, Z.-H.; Tian, Y.; Wang, S.-W.; Sun, Y.-C.; Wang, K.; Wang, W.; Zhang, Z.-F.; Liu, J.; Liu, Z.-T. Mass-Transfer Enhancement in the CO_2 Oxidative Dehydrogenation of Propane over GaN Supported on Zeolite Nanosheets with a Short B-Axis and Hierarchical Pores. *ACS Catal.* **2024**, *14*, 10376–10391.
[32] Li, L.-Y.; Wang, Z.-Y.; Yang, S.-Y.; Chen, J.-G.; He, Z.-H.; Wang, K.; Luo, Q.-X.; Liu, Z.-W.; Liu, Z.-T. Understanding the Role of Fe Doping in Tuning the Size and Dispersion of GaN Nanocrystallites for CO_2-Assisted Oxidative Dehydrogenation of Propane. *ACS Catal.* **2022**, *12*, 8527–8543.
[33] Zhang, L.; Wang, Z.-Y.; Song, J.; Lang, Y.; Chen, J.-G.; Luo, Q.-X.; He, Z.-H.; Wang, K.; Liu, Z.-W.; Liu, Z.-T. Facile Synthesis of SiO_2 Supported GaN as an Active Catalyst for CO_2 Enhanced Dehydrogenation of Propane. *J. CO_2 Util.* **2020**, *38*, 306–313.
[34] Yu, X.-Y.; Huang, Z.-Q.; Ban, T.; Xu, Y. H.; Liu, Z.-W.; Chang, C.-R. Finding Natural, Dense, and Stable Frustrated Lewis Pairs on Wurtzite Crystal Surfaces for Small-Molecule Activation. *Angew. Chem. Int. Ed.* **2024**, *63*, e202405405.
[35] Liu, C.; Kang, J.; Huang, Z.-Q.; Song, Y.-H.; Xiao, Y.-S.; Song, J.; He, J.-X.; Chang, C.-R.; Ge, H.-Q.; Wang, Y.; Liu, Z.-T.; Liu, Z.-W. Gallium Nitride Catalyzed the Direct Hydrogenation of Carbon Dioxide to Dimethyl Ether as Primary Product. *Nat. Commun.* **2021**, *12*, 2305.
[36] Yu, X.-Y.; Ban, T.; Su, X.; Huang, Z.-Q.; Chang, C.-R. Understanding the Facile Heterolytic Dissociation of Hydrogen on Natural Surface Frustrated Lewis Pairs. *J. Phys. Chem. C* **2023**, *127*, 15139–15147.
[37] Yu, X.-Y.; Su, X.; Xi, M.-J.; Huang, Z.-Q.; Chang, C.-R. Natural Surface Frustrated Lewis Pairs: The Concept and Beyond. *Chem. Asian J.* **2025**, *20*, e202401155.
[38] Bermudez, V. M. The Fundamental Surface Science of Wurtzite Gallium Nitride. *Surf. Sci. Rep.* **2017**, *72*, 147–315.
[39] Dreyer, C. E.; Janotti, A.; Van de Walle, C. G. Absolute Surface Energies of Polar and Nonpolar Planes of GaN. *Phys. Rev. B* **2014**, *89*, 081305.
[40] Song, Y.; Wu, X.; Wang, W.; Yuan, W.; Chen, X. Thermal Stability and Electronic Specific Heat of GaN. *J. Alloy. Compd.* **2004**, *370*, 65-68.
[41] Ambacher, O.; Brandt, M.; Dimitrov, R.; Metzger, T.; Stutzmann, M.; Fischer, R.; Miehr, A.; Bergmaier, A.; Dollinger, G. Thermal Stability and Desorption of Group III Nitrides Prepared by Metal Organic Chemical Vapor Deposition. *J. Vac. Sci. Technol. B* **1996**, *14*, 3532-3542.
[42] Nam, J.; Celik, F. E. Effect of Tin in the Bulk of Platinum–Tin Alloys for Ethane Dehydrogenation. *Top. Catal.* **2020**, *63*, 700–713.
[43] Nakaya, Y.; Hirayama, J.; Yamazoe, S.; Shimizu, K. I.; Furukawa, S. Single-Atom Pt in Intermetallics as an Ultrastable and Selective Catalyst for Propane Dehydrogenation. *Nat. Commun.* **2020**, *11*, 2838.
[44] Li, L.; Mu, X.; Liu, W.; Kong, X.; Fan, S.; Mi, Z.; Li, C.-J. Thermal Non-Oxidative Aromatization of Light Alkanes Catalyzed by Gallium Nitride. *Angew. Chem. Int. Ed.* **2014**, *53*, 14106–14109.
[45] Zhang, W.; Li, J.; Hui, L.; Gong, T.; Qin, L.; Lu, J.; Feng, H. Mesoporous Silica Supported Highly Dispersed GaN Catalysts Synthesized by Thermal Atomic Layer Deposition for Propane Dehydrogenation. *ChemCatChem* **2022**, *14*, e202200406.
[46] Liu, Y.; Zong, X.; Patra, A.; Caratzoulas, S.; Vlachos, D. G. Propane Dehydrogenation on Ptxsny (X, Y ≤ 4) Clusters on Al_2O_3(110). *ACS Catal.* **2023**, *13*, 2802–2812.
[47] Ma, H.-Y.; Wang, G.-C. Propane Dehydrogenation over Pd-Bi Intermetallic Compounds: A DFT Combined with Microkinetic Modeling Study. *Mol. Catal.* **2024**, *563*, 114253.
[48] Yang, M.-L.; Zhu, J.; Zhu, Y.-A.; Sui, Z.-J.; Yu, Y.-D.; Zhou, X.-G.; Chen, D. Tuning Selectivity and Stability in Propane Dehydrogenation by Shaping Pt Particles: A Combined Experimental and DFT Study. *J. Mol. Catal. A-Chem.* **2014**, *395*, 329–336.
[49] Nykänen, L.; Honkala, K. Selectivity in Propene Dehydrogenation on Pt and Pt_3Sn Surfaces from First Principles. *ACS Catal.* **2013**, *3*, 3026–3030.
[50] Saerens, S.; Sabbe, M. K.; Galvita, V. V.; Redekop, E. A.; Reyniers, M.-F.; Marin, G. B. The Positive Role of Hydrogen on the Dehydrogenation of Propane on Pt(111). *ACS Catal.* **2017**, *7*, 7495–7508.
[51] Zhu, J.; Yang, M.-L.; Yu, Y.; Zhu, Y.-A.; Sui, Z.-J.; Zhou, X.-G.; Holmen, A.; Chen, D. Size-Dependent Reaction Mechanism and Kinetics for Propane Dehydrogenation over Pt Catalysts. *ACS Catal.* **2015**, *5*, 6310–6319.
[52] Sokolov, S.; Stoyanova, M.; Rodemerck, U.; Linke, D.; Kondratenko, E. V. Comparative Study of Propane Dehydrogenation over V-, Cr-, and Pt-Based Catalysts: Time on-Stream Behavior and Origins of Deactivation. *J. Catal.* **2012**, *293*, 67–75.

Electronic Supplementary Material

Cooperation of frustrated Ga···N and Ga···Ga pairs on GaN breaks the linear scaling relationship in propane dehydrogenation

Xi-Yang Yu[1], Han-Xuan Liu[1], Han-Tao Cheng[1], Zheng-Qing Huang[1], and Chun-Ran Chang[1,2] ✉

[1] *State Key Laboratory of Fluorine & Nitrogen Chemicals, School of Chemical Engineering and Technology, Xi'an Jiaotong University, Xi'an 710049, China*
[2] *National Innovation Platform (Center) for Industry-Education Integration of Energy Storage Technology, Xi'an Jiaotong University, Xi'an 710049, China*

✉ Address correspondence to changcr@mail.xjtu.edu.cn

Supporting information to https://doi.org/10.26599/NR.2026.94908714

Computational details

First-Principles Calculations

All the spin-polarized density functional theory (DFT) calculations were performed using Vienna Ab initio Simulation Package (VASP).[1-3] The projector-augmented wave (PAW) method was adopted to describe electron-ion interactions.[4] The Perdew-Burke-Ernzerhof (PBE) functional within the generalized gradient approximation (GGA) framework was employed to treat exchange-correlation effects.[5] The DFT + *U* method was implemented for Ga 3*d* orbital, with an effective *U* parameter of 3.9 eV.[6] Van der Waals (vdW) interactions were accounted for using Grimme's D3 dispersion correction with zero damping.[7] A plane-wave cutoff energy of 400 eV was employed for all the calculation, and the Brillouin zone was sampled using a Γ-centered *k*-point grid of 2 × 2 × 1 for the GaN(100) surface.[8] The GaN(100) surface was modeled as a 3 × 2 supercell with six atomic layers. The Pt_3Sn(111) surface was modeled using a four-layer slab with a 4 × 4 supercell, with a Γ-centered 3 × 3 × 1 Monkhorst–Pack *k*-point mesh. The bottom two atomic layers were fixed, and a vacuum layer of 15 Å was introduced along the surface normal. Dipole corrections were applied in the same direction. The electronic relaxation reaches converged when the total energy change between successive steps fell below 10^{-5} eV, and ionic optimizations proceeded until forces on all atoms were less than 0.02 eV/Å. Gaussian smearing with a width of 0.05 eV was applied. The atomic charges were analyzed via Bader charge analysis.[9] Transition states (TS) were located using a combination of the nudged elastic band (NEB) and the dimer method.[10, 11] All identified transition states were verified by vibrational frequency analysis. Each transition state exhibits a single imaginary frequency corresponding to the reaction coordinate.

The Gibbs free energy (*G*) was calculated by using the following formula:

$$G = E_{\mathrm{DFT}} + E_{\mathrm{ZPE}} + H - TS$$

where E_{DFT} is the electronic energy obtained by DFT calculations, E_{ZPE} is the zero-point energy correction that is computed from vibrational frequencies, *H* is the change of enthalpy from 0 K to 873 K, T*S* is the temperature-entropy term, calculated as temperature multiplied by the entropy.

The total entropy can be divided into three main parts: translational entropy (S_t), rotational entropy (S_r), and vibrational entropy (S_v), as follows:

$$S = S_t + S_r + S_v$$

The formulas for S_t, S_r, and S_v are given below:

$$S_t = R\left(\ln\left(\left(\frac{2\pi m k_B T}{h^2}\right)^{3/2}\frac{k_B T}{P}\right)+\frac{5}{2}\right)$$

$$S_r = R\ln\left(\frac{\pi^{1/2}}{\sigma_r}\left(\frac{T^{3/2}}{\left(\frac{\hbar^2}{2I_x k_B}\frac{\hbar^2}{2I_y k_B}\frac{\hbar^2}{2I_z k_B}\right)^{1/2}}\right)+\frac{3}{2}\right)$$

$$S_v = R\sum_k\left(\frac{h\nu_K/k_B T}{e^{(h\nu_K/k_B T)}-1}-\ln\left[1-e^{-(h\nu_K/k_B T)}\right]\right)$$

In the harmonic approximation, E_{ZPE} and the *H* are expressed as follows:

$$E_{ZPE} = \frac{1}{2}R\sum_k\frac{h\nu_K}{k_B}$$

$$H = 3RT + R\sum_k\left(\frac{h\nu_K}{k_B}\frac{1}{e^{(h\nu_K/k_B T)}-1}\right)+k_B T$$

In the above equations, k_B is the Boltzmann constant, h is the Planck constant, $\hbar$ is the reduced Planck constant, R is the ideal gas constant, m is the molecular mass, T is temperature, σ_r is the rotational symmetry number, I_i (i = x, y, and z) are the principal moments of inertia, and ν_k is the harmonic vibrational frequency of the k^{th} normal mode.

The Gibbs free energy of reaction (ΔG) was calculated as the difference between the final states (FS) and initial states (IS):

$$\Delta G = G_{FS} - G_{IS}$$

The Gibbs free energy of activation (G_a) was defined as the difference between the TS and IS:

$$G_a = G_{TS} - G_{IS}$$

The negative projected crystal orbital Hamiltonian population (–pCOHP) curves were calculated using LOBSTER with the pbeVASPfit2015 basis set, achieving accurate projection (charge spilling < 1%).[12, 13]

Microkinetic Simulation Methods

The kMC simulation was carried out using the kinetic Monte Carlo of systems (kMCos) software package.[14] The catalytic performance of GaN for propane dehydrogenation was evaluated based on a constructed reaction network, as shown in Tables S1 and S2. The network includes all elementary steps of the reaction, including propane adsorption, C–H bond cleavage, propylene desorption, and potential coke formation. The rate constants for each elementary step were calculated from the corresponding Gibbs free energy barriers using the Arrhenius equation:

$$k = \frac{k_B T}{h} exp\left(-\frac{G_a}{k_B T}\right)$$

where k is the rate constant, k_B is the Boltzmann constant, h is the Planck constant, and T is the reaction temperature.

The rate constant for non-activated gas adsorption is given by:

$$k = \frac{P_i A}{\sqrt{2\pi m k_B T}}$$

where P_i is the partial pressure of gas i, A is the effective area of the site where the reaction takes place, m is mass of the molecule i, k_B is the Boltzmann constant, and h is the Planck constant.

The rate constants for desorption were calculated as follows:

$$k = \frac{k_B T}{h} exp\left(-\frac{\Delta G}{k_B T}\right)$$

where ΔG is the Gibbs free energy change for desorption.

The turnover frequency (TOF) was calculated from the steady-state kMC trajectory as the average number of propylene molecules produced per active site per second, as follows:

$$TOF = \frac{N(C_3H_6)}{N_{site} \times t}$$

where $N(C_3H_6)$ is the number of propylene molecules formed, N_{site} is the number of active sites in the model, and t is the simulation time.

The surface sites were represented by the Ga and N atoms in the topmost layer of the GaN(100) surface. Ga atoms can form Ga···N FLPs with next-nearest-neighbor N atoms, or Ga···Ga pairs with nearest-neighbor Ga atoms, allowing the kMC simulations to account for both types of active centers and their spatial distribution. A surface model consisting of 20 × 20 unit cells was employed in these simulations. The turnover frequency (TOF) was computed over sufficiently long simulation steps (10^{11}) to ensure convergence, providing a quantitative assessment of both catalytic activity and selectivity. Lateral interactions were not included in the kMC model, as the surface coverage is expected to be low under the high-temperature conditions. The simulation temperature was set to 873 K and the pressure of propane to 1 bar.

Ab Initio Molecular Dynamics Simulations

To investigate specific elementary steps at the reaction temperature, constrained ab initio molecular dynamics (AIMD) simulations were performed using the CP2K 7.1 package.[15] The electronic structure was described using DFT with the PBE functional and the DZVP-MOLOPT-SR-GTH basis set, with a plane-wave cutoff of 400 eV. The system was modeled in the NVT ensemble, with temperature maintained by a Nosé–Hoover chain thermostat, and a time step of Δt = 0.5 fs.[16, 17] The constraints were enforced from the start of the AIMD simulations using harmonic potentials along the defined collective variables (CVs). For the first C–H bond cleavage, the CVs were chosen as the distance between the Ga atom and the adsorbed carbon atom of propane (Ga···C) and the distance between the N atom and the adsorbed hydrogen atom (N···H), capturing the cooperation of the FLPs (Figure 3). For

the subsequent dehydrogenation of the propyl intermediate to propene, the CVs were chosen as the $Ga_I \cdots C_I$ and $Ga_{II} \cdots H_I$ distances (Figure 4).

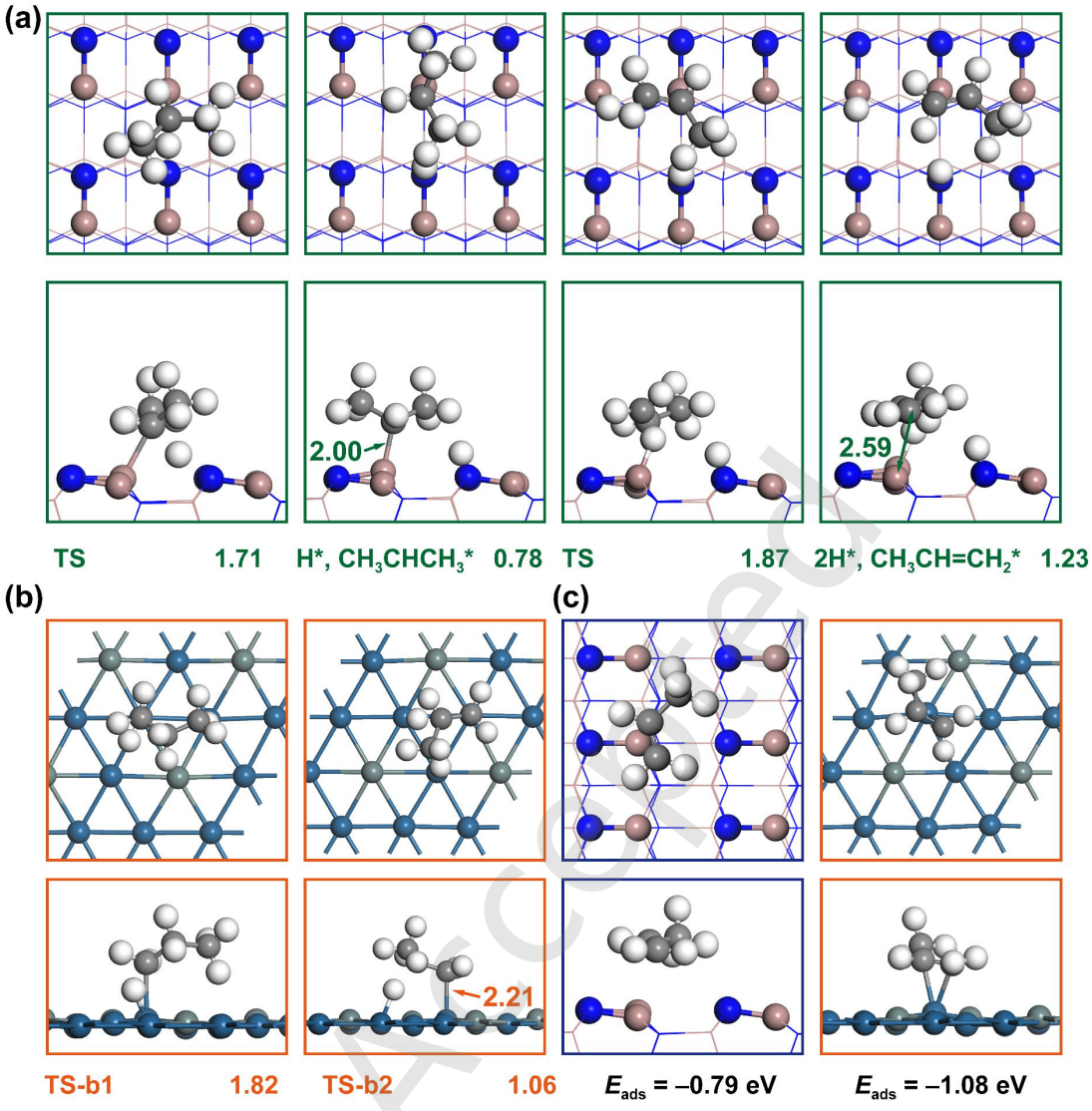

Figure S1. Optimized intermediate and TS structures on the (a) GaN(100) and (b) $Pt_3Sn(111)$ for propane dehydrogenation. (c) Propylene adsorption configuration on GaN(100) and $Pt_3Sn(111)$ surfaces. The numbers below the structures denote the corresponding energies (in eV), and those inside the boxes represent the distances (in Å).

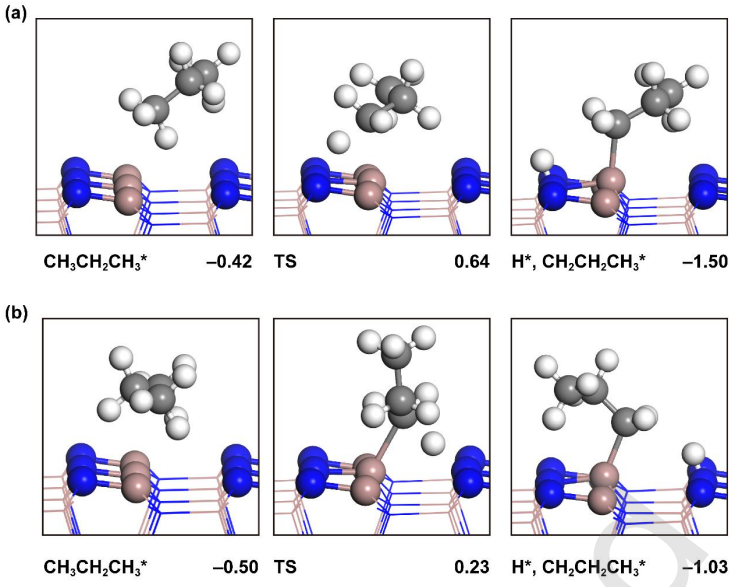

Figure R2. Optimized intermediate and TS structures for propane dehydrogenation at (a) CLPs and (b) FLPs on GaN(100). The numbers below the structures represent the corresponding energies, with units of eV.

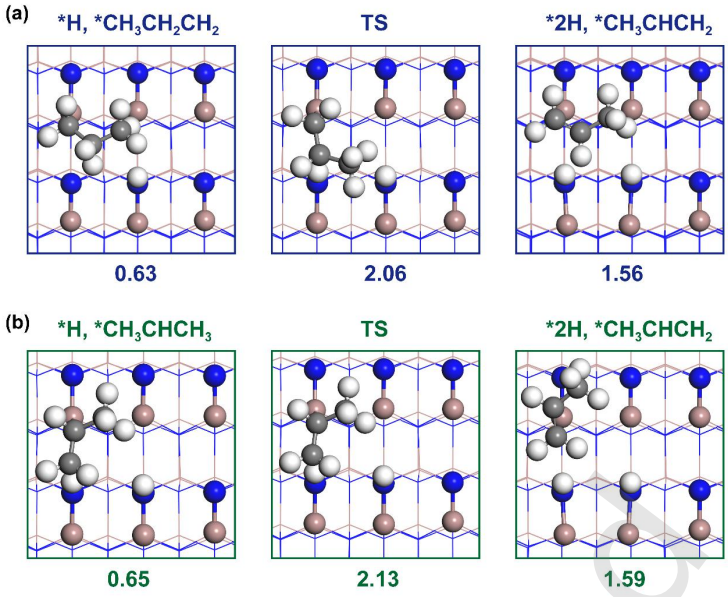

Figure S3. Optimized structures for the dehydrogenation of (a) 1-propyl and (b) 2-propyl to propylene on the GaN(100) surface. The numbers below the structures represent the corresponding Gibbs free energies, with units of eV.

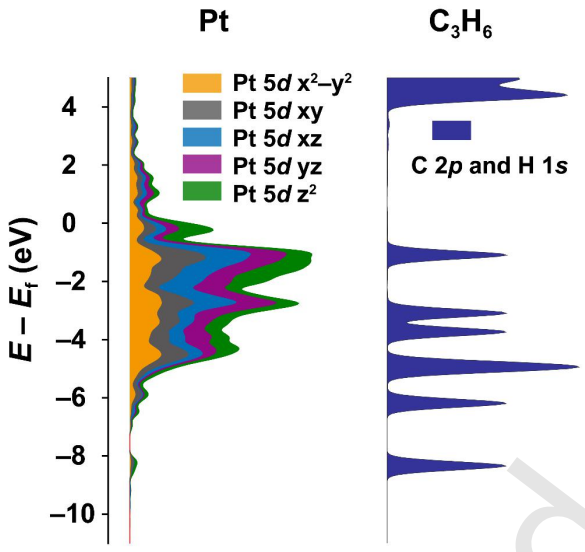

Figure S4. PDOS of the Pt 5*d* orbitals on the clean $Pt_3Sn(111)$ surface and the C 2*p* and H 1*s* orbitals of C_3H_6.

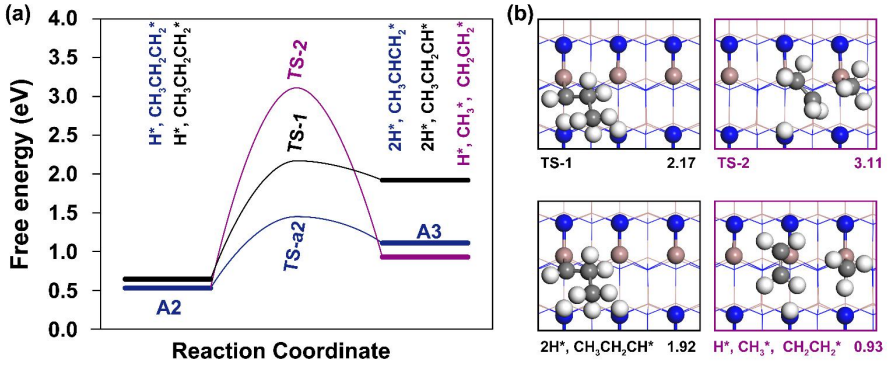

Figure S5. (a) Potential energy diagram for the deep dehydrogenation and C–C bond cleavage of 1-propyl. (b) Optimized intermediate and TS structures, with energies (in eV) shown below each structure.

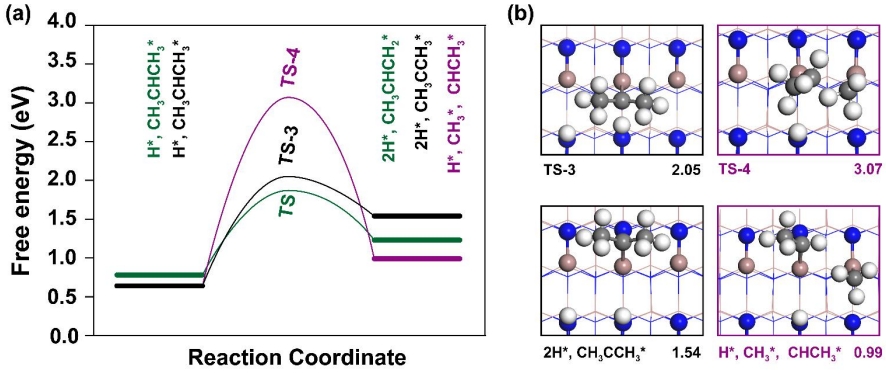

Figure S6. (a) Potential energy diagram for the deep dehydrogenation and C–C bond cleavage of 2-propyl. (b) Optimized intermediate and TS structures, with energies (in eV) shown below each structure.

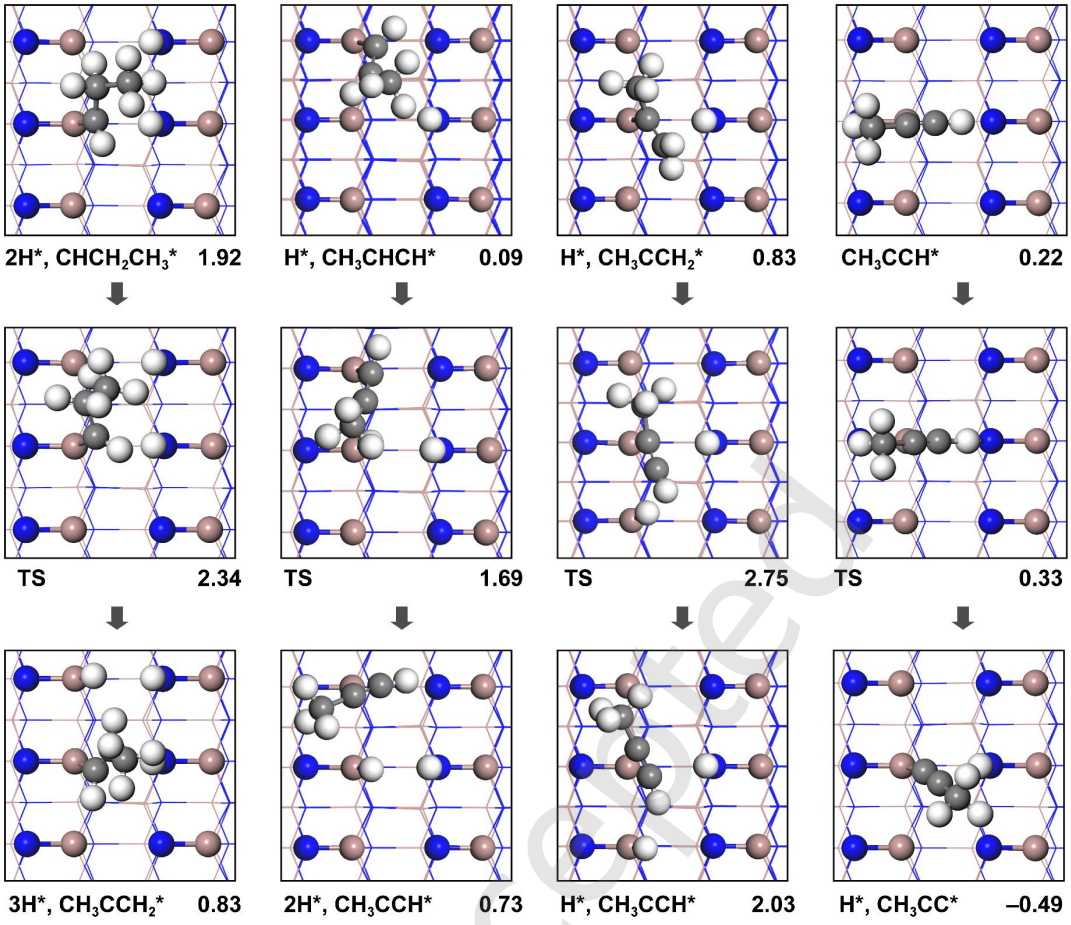

Figure S7. Optimized structures on the GaN(100) surface for deep dehydrogenation of C3 intermediates. The zero-energy reference corresponds to the Gibbs free energies of H_2(g), C_3H_8(g), and the GaN(100) surface. The numbers below the structures represent the corresponding Gibbs free energies, with units of eV.

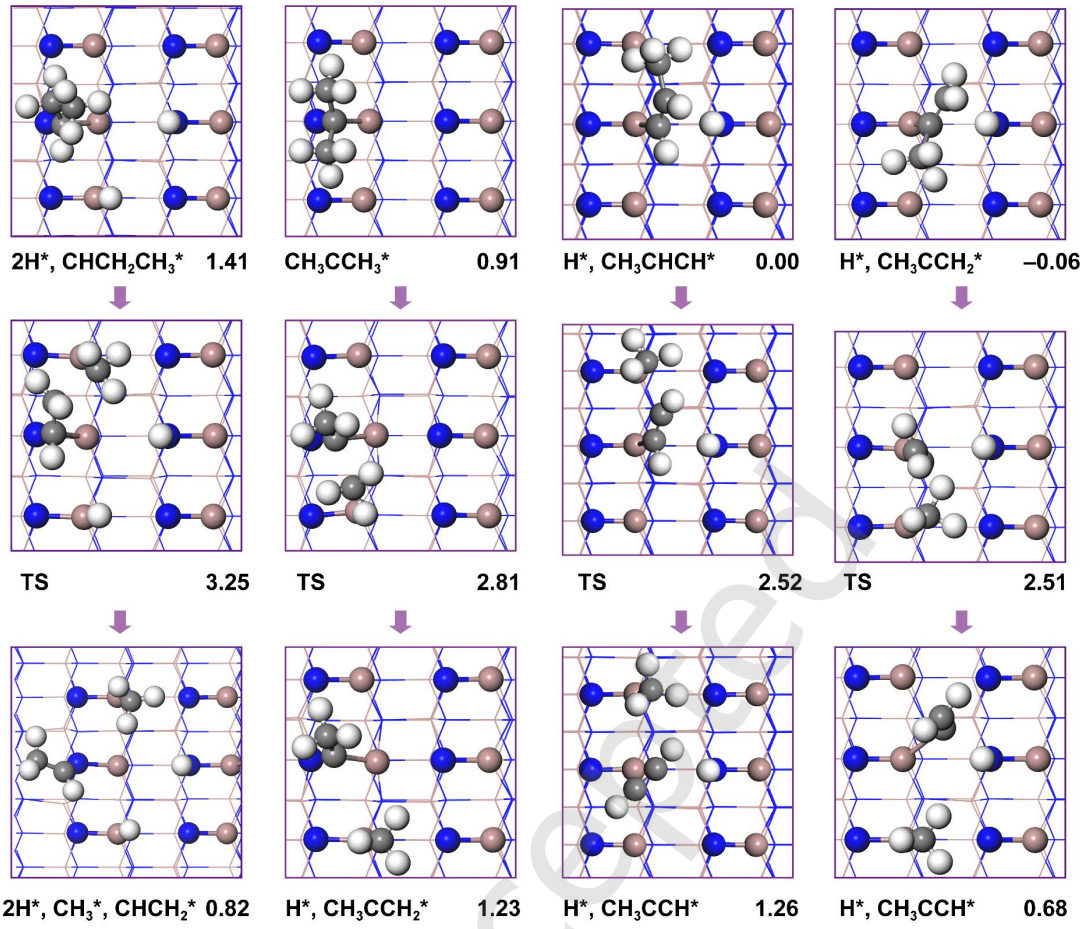

Figure S8. Optimized structures on the GaN(100) surface for C–C bond cleavage of C3 intermediates. The zero-energy reference corresponds to the Gibbs free energies of H_2(g), C_3H_8(g), and the GaN(100) surface. The numbers below the structures represent the corresponding Gibbs free energies, with units of eV.

Table S1. Gibbs Free Energy of Activation and Gibbs Free Energy of Reaction for the Elementary Reactions Involving C_3 Species

	Surface Reaction	ΔG (eV)	G_a (eV)
R1	$CH_3CH_2CH_3(g) \rightarrow CH_3CH_2CH_2^* + H^*$	0.53	1.63
R2	$CH_3CH_2CH_2^* \rightarrow CH_3CH{=}CH_2^* + H^*$	0.48	0.92
R3	$CH_3CH{=}CH_2^* \rightarrow CH_3CH{=}CH_2(g) + *$	–1.23	
R4	$CH_3CH_2CH_3^* \rightarrow CH_3CHCH_3^* + H^*$	0.78	1.71
R5	$CH_3CHCH_3^* \rightarrow CH_3CH{=}CH_2^* + H^*$	0.26	1.09
R6	$CH_3CH{=}CH_2^* \rightarrow CH_3CH{=}CH_2(g) + *$	–1.16	
R7	$CH_3CH{=}CH_2^* \rightarrow CH_3CH{=}CH^* + H^*$	–0.31	0.56
R8	$CH_3CH{=}CH^* \rightarrow CH_3C{\equiv}CH^* + H^*$	0.64	1.60
R9	$CH_3CH{=}CH_2^* \rightarrow CH_3C{=}CH_2^* + H^*$	0.21	0.80
R10	$CH_3C{=}CH_2^* \rightarrow CH_3C{\equiv}CH^* + H^*$	1.20	1.92
R11	$CH_3CH{=}CH_2(g) + 2^* \rightarrow CH_3CH{=}CH_2^{**}$	0.92	
R12	$CH_3CH{=}CH_2^{**} \rightarrow CH_3C{=}CH_2^{**} + H^*$	0.96	1.77
R13	$CH_3C{=}CH_2^{**} \rightarrow CH_3C{=}CH_2^* + *$	–0.90	
R14	$CH_3C{\equiv}CH^* \rightarrow CH_3C{\equiv}CH\ (g) + *$	–1.06	
R15	$CH_3C{\equiv}CH^* + * \rightarrow CH_3C{\equiv}C^* + H^*$	–0.71	0.11
R16	$CH_3CH_2CH_2^* \rightarrow CH_3CH_2CH^* + H^*$	0.93	2.45
R17	$CH_3CH_2CH^* \rightarrow CH_3CH{=}CH^* + H^*$	–1.09	0.42
R18	$CH_3CHCH_3^* \rightarrow CH_3CCH_3^* + H^*$	0.90	1.41
R19	$CH_3CCH_3^* \rightarrow CH_3C{=}CH_2^* + H^*$	–0.97	0.00
R20	$CH_3CH_2CH_2^* \rightarrow CH_2{=}CH_2^* + CH_3^*$	0.40	2.58
R21	$CH_3CH_2CH^* \rightarrow CH_2{=}CH^* + CH_3^*$	–0.59	1.84
R22	$CH_3CH{=}CH^* \rightarrow CH{\equiv}CH^* + CH_3^*$	1.26	2.52
R23	$CH_3CHCH_3^* \rightarrow CHCH_3^* + CH_3^*$	0.35	2.43
R24	$CH_3CCH_3^* \rightarrow CCH_3^* + CH_3^*$	0.32	1.90
R25	$CH_3C{=}CH_2^* \rightarrow C{=}CH_2^* + CH_3^*$	0.74	2.57

Table S2. Gibbs Free Energy of Activation and Gibbs Free Energy of Reaction for the Elementary Reactions Involving C_1, C_2, and H Species

	Surface Reaction	ΔG (eV)	G_a (eV)
R26	$CH_3^* \rightarrow CH_2^* + H^*$	1.23	3.01
R27	$CH_2^* \rightarrow CH^* + H^*$	1.48	2.47
R28	$CH^* \rightarrow C^* + H^*$	0.60	1.71
R29	$CH_3^* + H^* \rightarrow CH_4^*$	0.19	0.94
R30	$CH_4^* \rightarrow * + CH_4(g)$	–1.04	
R31	$CH_2{=}CH_2^* \rightarrow CH_2{=}CH_2(g) + *$	–1.13	
R32	$CH_2{=}CH_2^* \rightarrow CH_2{=}CH^* + H^*$	–0.15	0.62
R33	$CH_2{=}CH^* \rightarrow CH{\equiv}CH^* + H^*$	0.97	1.61
R34	$CH{\equiv}CH^* \rightarrow C{\equiv}CH^* + H^*$	–0.84	0.12
R35	$C{\equiv}CH^* \rightarrow C{\equiv}C^* + H^*$	1.20	4.16
R36	$H^* + H^* \rightarrow H_2^*$	0.72	1.04
R37	$H_2^* \rightarrow H_2(g) + *$	–1.27	

Table S3. Activation Barriers and Reaction Energies for the Surface Reactions of C_3 Species

	Surface Reaction	ΔE (eV)	E_a (eV)
R1	$CH_3CH_2CH_3(g) \rightarrow CH_3CH_2CH_2^* + H^*$	–0.53	0.23
R2	$CH_3CH_2CH_2^* \rightarrow CH_3CH{=}CH_2^* + H^*$	0.83	1.00
R3	$CH_3CH{=}CH_2^* \rightarrow CH_3CH{=}CH_2(g) + *$	0.79	
R4	$CH_3CH_2CH_3^* \rightarrow CH_3CHCH_3^* + H^*$	–0.50	0.27
R5	$CH_3CHCH_3^* \rightarrow CH_3CH{=}CH_2^* + H^*$	0.77	1.29
R6	$CH_3CH{=}CH_2^* \rightarrow CH_3CH{=}CH_2(g) + *$	0.74	
R7	$CH_3CH{=}CH_2^* \rightarrow CH_3CH{=}CH^* + H^*$	–0.46	0.49
R8	$CH_3CH{=}CH^* \rightarrow CH_3C{\equiv}CH^* + H^*$	0.92	1.61
R9	$CH_3CH{=}CH_2^* \rightarrow CH_3C{=}CH_2^* + H^*$	0.45	0.64
R10	$CH_3C{=}CH_2^* \rightarrow CH_3C{\equiv}CH^* + H^*$	0.92	2.01
R11	$CH_3CH{=}CH_2(g) + 2^* \rightarrow CH_3CH{=}CH_2^{**}$	–1.51	
R12	$CH_3CH{=}CH_2^{**} \rightarrow CH_3C{=}CH_2^{**} + H^*$	1.29	1.98
R13	$CH_3C{=}CH_2^{**} \rightarrow CH_3C{=}CH_2^* + *$	–1.05	
R14	$CH_3C{\equiv}CH^* \rightarrow CH_3C{\equiv}CH\ (g) + *$	1.11	
R15	$CH_3C{\equiv}CH^* + * \rightarrow CH_3C{\equiv}C^* + H^*$	–0.73	0.16
R16	$CH_3CH_2CH_2^* \rightarrow CH_3CH_2CH^* + H^*$	0.85	2.59
R17	$CH_3CH_2CH^* \rightarrow CH_3CH{=}CH^* + H^*$	–0.37	0.99
R18	$CH_3CHCH_3^* \rightarrow CH_3CCH_3^* + H^*$	0.75	1.53
R19	$CH_3CCH_3^* \rightarrow CH_3C{=}CH_2^* + H^*$	–0.77	0.00
R20	$CH_3CH_2CH_2^* \rightarrow CH_2{=}CH_2^* + CH_3^*$	0.73	2.60
R21	$CH_3CH_2CH^* \rightarrow CH_2{=}CH^* + CH_3^*$	–0.50	1.82
R22	$CH_3CH{=}CH^* \rightarrow CH{\equiv}CH^* + CH_3^*$	1.71	2.65
R23	$CH_3CHCH_3^* \rightarrow CHCH_3^* + CH_3^*$	0.35	2.41
R24	$CH_3CCH_3^* \rightarrow CCH_3^* + CH_3^*$	0.52	1.96
R25	$CH_3C{=}CH_2^* \rightarrow C{=}CH_2^* + CH_3^*$	0.74	2.66

Table S4. Activation Barriers and Reaction Energies for Surface Reactions of C_1, C_2, and H Species

	Surface Reaction	ΔE (eV)	E_a (eV)
R26	$CH_3^* \rightarrow CH_2^* + H^*$	0.92	2.88
R27	$CH_2^* \rightarrow CH^* + H^*$	1.58	2.85
R28	$CH^* \rightarrow C^* + H^*$	0.75	1.73
R29	$CH_3^* + H^* \rightarrow CH_4^*$	0.68	1.30
R30	$CH_4^* \rightarrow * + CH_4(g)$	0.27	
R31	$CH_2{=}CH_2^* \rightarrow CH_2{=}CH_2(g) + *$	0.66	
R32	$CH_2{=}CH_2^* \rightarrow CH_2{=}CH^* + H^*$	–0.55	0.53
R33	$CH_2{=}CH^* \rightarrow CH{\equiv}CH^* + H^*$	1.25	1.79
R34	$CH{\equiv}CH^* \rightarrow C{\equiv}CH^* + H^*$	–0.97	0.13
R35	$C{\equiv}CH^* \rightarrow C{\equiv}C^* + H^*$	0.96	4.18
R36	$H^* + H^* \rightarrow H_2^*$	1.10	1.20
R37	$H_2^* \rightarrow H_2(g) + *$	0.18	

The activation energies of CH_4^*, $CH_2{=}CH_2^*$, and $CH_2{=}CH^*$ are taken from our previous studies.[18, 19]

Refernece

[1] Kresse, G.; Furthmüller, J. Efficiency of Ab-Initio Total Energy Calculations for Metals and Semiconductors Using a Plane-Wave Basis Set. *Comput. Mater. Sci.* **1996**, *6*, 15-50.

[2] Kresse, G.; Furthmüller, J. Efficient Iterative Schemes for Ab Initio Total-Energy Calculations Using a Plane-Wave Basis Set. *Phys. Rev. B* **1996**, *54*, 11169-11186.

[3] Kresse, G.; Hafner, J. Ab Initio Molecular-Dynamics Simulation of the Liquid-Metal-Amorphous-Semiconductor Transition in Germanium. *Phys. Rev. B* **1994**, *49*, 14251-14269.

[4] Kresse, G.; Joubert, D. From Ultrasoft Pseudopotentials to the Projector Augmented-Wave Method. *Phys. Rev. B* **1999**, *59*, 1758-1775.

[5] John P. Perdew, K. B., Matthias Ernzerhof Generalized Gradient Approximation Made Simple. *Phys. Rev. Lett.* **1996**, *77*, 3865-3868.

[6] Jensen, L. L.; Muckerman, J. T.; Newton, M. D. First-Principles Studies of the Structural and Electronic Properties of the $(Ga_{1-x}Zn_x)(N_{1-x}O_x)$ Solid Solution Photocatalyst. *J. Phys. Chem. C* **2008**, *112*, 3439-3446.

[7] Grimme, S.; Antony, J.; Ehrlich, S.; Krieg, H. A Consistent and Accurate Ab Initio Parametrization of Density Functional Dispersion Correction (DFT-D) for the 94 Elements H-Pu. *J. Chem. Phys.* **2010**, *132*, 154104.

[8] Monkhorst, H. J.; Pack, J. D. Special Points for Brillouin-Zone Integrations. *Phys. Rev. B* **1976**, *13*, 5188-5192.

[9] Bader, R. F. W. A Quantum Theory of Molecular Structure and Its Applications. *Chem. Rev.* **1991**, *91*, 893-928.

[10] Henkelman, G.; Jonsson, H. A Dimer Method for Finding Saddle Points on High Dimensional Potential Surfaces Using Only First Derivatives. *J. Chem. Phys.* **1999**, *111*, 7010-7022.

[11] Jónsson, H.; Mills, G.; Jacobsen, K. W. *In Classical and Quantum Dynamics in Condensed Phase Simulations*; World Scientific: Singapore, 1998.

[12] Dronskowski, R.; Bloechl, P. E. Crystal Orbital Hamilton Populations (COHP): Energy-Resolved Visualization of Chemical Bonding in Solids Based on Density-Functional Calculations. *J. Phys. Chem. B* **1993**, *97*, 8617-8624.

[13] Maintz, S.; Deringer, V. L.; Tchougréeff, A. L.; Dronskowski, R. LOBSTER: A Tool to Extract Chemical Bonding from Plane-Wave Based DFT. *J. Comput. Chem.* **2016**, *37*, 1030-1035.

[14] Hoffmann, M. J.; Matera, S.; Reuter, K. Kmos: A Lattice Kinetic Monte Carlo Framework. *Comput. Phys. Commun.* **2014**, *185*, 2138-2150.

[15] Kuhne, T. D.; Iannuzzi, M.; Del Ben, M.; Rybkin, V. V.; Seewald, P.; Stein, F.; Laino, T.; Khaliullin, R. Z.; Schutt, O.; Schiffmann, F.; Golze, D.; Wilhelm, J.; Chulkov, S.; Bani-Hashemian, M. H.; Weber, V.; Borstnik, U.; Taillefumier, M.; Jakobovits, A. S.; Lazzaro, A.; Pabst, H.; Muller, T.; Schade, R.; Guidon, M.; Andermatt, S.; Holmberg, N.; Schenter, G. K.; Hehn, A.; Bussy, A.; Belleflamme, F.; Tabacchi, G.; Gloss, A.; Lass, M.; Bethune, I.; Mundy, C. J.; Plessl, C.; Watkins, M.; VandeVondele, J.; Krack, M.; Hutter, J. CP2K: An Electronic Structure and Molecular Dynamics Software Package - Quickstep: Efficient and Accurate Electronic Structure Calculations. *J. Chem. Phys.* **2020**, *152*, 194103.

[16] Nosé, S. A Unified Formulation of the Constant Temperature Molecular Dynamics Methods. *J. Chem. Phys.* **1984**, *81*, 511-519.

[17] Hoover, W. G. Canonical Dynamics: Equilibrium Phase-Space Distributions. *Phys. Rev. A* **1985**, *31*, 1695-1697.

[18] Yu, X.-Y.; Huang, Z.-Q.; Ban, T.; Xu, Y. H.; Liu, Z.-W.; Chang, C.-R. Finding Natural, Dense, and Stable Frustrated Lewis Pairs on Wurtzite Crystal Surfaces for Small-Molecule Activation. *Angew. Chem. Int. Ed.* **2024**, *63*, e202405405.

[19] Yu, X.-Y.; Ban, T.; Su, X.; Huang, Z.-Q.; Chang, C.-R. Understanding the Facile Heterolytic Dissociation of Hydrogen on Natural Surface Frustrated Lewis Pairs. *J. Phys. Chem. C* **2023**, *127*, 15139–15147.